Characterizing heterogeneities in the subsurface with an ultra-wideband GPR: Application to WISDOM, the GPR of the Rosalind Franklin ExoMars mission

Emile Brighi, Valérie Ciarletti, Alice Le Gall, D Plettemeier, Yann Herve, Nicolas Oudart, C Quantin-Nataf, Manon Gilles, François-Wandrille de Lamberterie

Planetary and Space Science 255 (2025) 106012

Contents lists available at ScienceDirect

Planetary and Space Science

journal homepage: www.elsevier.com/locate/pss

Characterizing heterogeneities in the subsurface with an ultra-wideband GPR: Application to WISDOM, the GPR of the Rosalind Franklin ExoMars mission

E. Brighi [a,*], V. Ciarletti [a], A. Le Gall [a], D. Plettemeier [c], Y. Hervé [a], N. Oudart [a], C. Quantin-Nataf [b], M. Gilles [a], F.-W. de Lamberterie [a]

[a] LATMOS/IPSL, UVSQ Université Paris-Saclay, Sorbonne Université, CNRS, France
[b] Université Claude Bernard Lyon 1: Villeurbanne, Auvergne-Rhône-Alpes, France
[c] Technische Universität Dresden, Dresden, Germany

ARTICLE INFO

Keywords:
Subsurface investigation
Ultra-wideband ground penetrating radar
Volume scattering
Mars

ABSTRACT

Ultra-wideband Ground Penetrating Radars (GPR) are sensitive to a large range of scatterer sizes. Considering fractal heterogeneities in the subsurface, we propose a method to retrieve their typical size L. The determination of L with this method does not require *a priori* knowledge of the statistical distribution of permittivity values in the investigated subsurface. The method relies on the analysis of the backscattered signal by frequency/wavelength sub-bands. It is adapted to WISDOM, the GPR onboard the rover of the Rosalind Franklin ExoMars mission (ESA), but can be applied to any ultra-wideband GPR. Based on numerical simulations, a maximum in volume backscattering is reached at the wavelength (in the subsurface) $\lambda = (5.3 \pm 0.2)L$. We demonstrate that this maximum, and therefore L, can be identified even in presence of moderate electrical losses, compatible with conditions expected on the Moon or Mars. Assuming an average permittivity of 5, WISDOM (0.5–3 GHz) data products could be used to estimate L as long as it is in the range 0.9–4.2 cm. The retrieval method for L is validated on experimental WISDOM data acquired in a controlled environment.

1. Introduction

Characterizing the subsurface provides substantive clues to reconstruct the geological history of a given area through the knowledge of its chemical composition and geophysical properties. In planetary science, with the notable exception of the Moon, this characterization relies on unmanned exploration. There are several ways to investigate the subsurface from instruments operating at the surface. Let us cite: (i) Visual inspection of outcrops, crater walls or canyons provides clues about the subsurface structures. (ii) Seismology can reveal the internal composition and structure of a planet at different scales (e.g., Lognonné et al., 2019) (iii) Drilling cores directly provides information on the shallow crust (typically the first meters below the surface) but is very local and destructive. Missions of robotic exploration including drilling operations have already been operating on Mars: (Farley et al., 2020; Spohn et al., 2018; Vasavada, 2022). (iv) Ground Penetrating Radars (GPR) which are now commonly accommodated on missions' rover (Farley et al., 2020; Li et al., 2015; Vago et al., 2017; Zou et al., 2021) can give access to the subsurface in a non-destructive manner down to depths commensurate with the operating wavelength/frequency. They are usually designed to sound a few meters to hundreds of meters below the surface depending on the scientific objectives of the mission. The present paper focuses on the investigation of the subsurface by GPR.

Clear buried interfaces or resolvable large reflecting structures are probably the most easily interpretable features a GPR can detect in the subsurface. However, radargrams -which are the primary products of a GPR and offer an image of the subsurface-most often display the signatures of diffuse scattering in the subsurface volume rather than clear structures. As an example, the radargram acquired by the Rover ground-Penetrating Radar (RoPeR) onboard the Zhurong rover of the China's Tianwen-1 mission at Utopia Planitia on Mars points to the presence in the subsurface of two layers containing scatterers of different size or nature, but no clear interface (Li et al., 2022). Scattering signature was also observed in the lunar subsurface by the LPR (Lunar Penetrating Radar) instruments on board the Yutu rovers of the China's Chang'e 3 (Lai et al., 2016) and Chang'e 4 missions (Zhang et al., 2020) and by

* Corresponding author.
E-mail address: emile.brighi@latmos.ipsl.fr (E. Brighi).

https://doi.org/10.1016/j.pss.2024.106012
Received 20 October 2023; Received in revised form 10 October 2024; Accepted 24 November 2024
Available online 30 November 2024

LRPR (Lunar Regolith Penetrating Radar) mounted on the China's Chang'e 5 lander (Li et al., 2022). In Jezero crater on Mars, the Radar Imager for Mars' Subsurface Experiment (RIMFAX) did reveal buried interfaces but also a great number of scattering features along the 3 km long path of the Perseverance rover of the Mars 2020 mission (NASA) (Hamran et al., 2022).

Scattering signatures indicates the presence of heterogeneities of size comparable to the observational wavelength of the GPR, either due to inclusions embedded in a substrate of different composition or to local subtle variations of the porosity or/and composition. For instance, heterogeneities could be pyroclastic, sedimentary (fluvial, glacial, aeolian) or ejecta deposits. Their size distribution and evolution with depth as well as their shape are essential to understand the origin and transport of materials in a given site of interest and therefore to trace back the local chronology of geological events.

For example, the images acquired by the Mars Science Laboratory (MSL) Mast Camera at Gale crater show rounded pebbles with properties indicative of the fluvial activity that caused their abrasion (Williams et al., 2013). A minimal transport distance of a few kilometers was estimated. The grain size distribution with a median size <1 cm and a maximum size of less than 10 cm was used to estimate the depth and the mean velocity of the flow.

In contrast, at Jezero crater, the Perseverance rover's cameras provided images of outcrops exposing a number of strata, some of them embedding conglomerates with pebbles significantly larger than those observed in Gale crater with a median value around 16.4 cm (Mangold et al., 2021). The interpretation of the observed stratigraphy calls for episodes of very energetic fluvial flows of short-duration.

Scattering signatures can also point to macro-porosity in the subsurface. For instance, volcanic rocks like vesicular basalts are made of millimetric to centimetric void vesicles which could act as efficient scatterers at GPR wavelengths. For terrestrial volcanoes, it has been demonstrated that the information on the bubble size distribution can be used to quantitatively retrieve parameters such as the saturation pressure and magma ascent velocity in the volcanic conduit (Blower et al., 2003).

So far, visual inspection was the primary mean to obtain clues on the local subsurface along a rover's path on Mars. In 2021, the Martian exploration entered a new era with the arrival of GPR operating from the surface. Indeed, a wealth of scientific results have been obtained very recently thanks to RIMFAX/Mars 2020 and RoPeR/Zhurong. For instance (Li et al., 2022), put constraints on the subsurface composition in Utopia Planitia (through the study of the variations of its permittivity with depth) while (Paige et al., 2024) show how revealing the stratigraphy of Jezero crater provides insights into the regional geological history.

The next GPR on Mars will likely be WISDOM (Water Ice Subsurface Deposits On Mars), an ultra-wide band radar (Ciarletti et al., 2011, 2017) designed for the ExoMars rover mission (Vago et al., 2017) recently rebaptized the ExoMars/Rosalind Franklin Mission (EXM/RFM). The main objective of the EXM/RFM mission is to find evidence of present or past life in the Martian subsurface, where organic molecules, if present, are shielded from the ionizing radiation and atmospheric oxidants. WISDOM will be on-board the Rosalind Franklin rover and investigate the first meters below the surface of the landing site, Oxia Planum (Quantin-Nataf et al., 2021), in order to understand its geological context and history. WISDOM investigation will also guide the drilling operations towards safe and scientifically-relevant locations where to sample subsurface material. Based on RIMFAX and RoPeR observations on Mars, WISDOM radargrams in Oxia Planum could prove to be difficult to interpret if the subsurface consists of a heterogenous medium including a large density of scattering structures of dimension commensurate with WISDOM wavelengths of operation. This idea is supported by field tests conducted on Earth with spare models of the WISDOM instrument, for instance in the Atacama Desert (Dorizon et al., 2014; Oudart, 2021), in the so-called "Colorado Provençal" in France (Hervé, 2018) or on Svalbard Island, Norway.

Characterizing subsurface heterogeneities using data acquired by GPR is challenging. Small-scale structures can result in overlapping radar signatures as strong reflections, diffractions, and interference patterns in GPR data, making the interpretation of radargrams difficult. Similar scattering radar responses can arise from different geological materials or structures, leading to ambiguity in data interpretation. Inverting these data involve solving a highly nonlinear inverse problem with non-unique solutions that fit the observed data equally well.

Several experimental studies investigated specific cases of small-scale permittivity variations. For instance (Rea and Knight, 1998) were able to determine the paleo-flow direction and the correlation length of a fine-grained lithological sedimentary structures through 2-D and 3-D correlation analysis of the GPR data (Van Dam et al., 2003). noticed qualitatively that interferences of the reflected signals in a subcentimeter-scale sedimentary layering change with the center frequency of narrow-band the GPR operating at 900 and 450 MHz (Dai et al., 2022). propose a two-stage deep learning-based method for GPR data inversion under heterogeneous soil conditions, but obtain results limited to the reconstruction of the shape, orientation and size of one to three 2-D objects buried in a 2-D simulated heterogeneous subsurface. Theoretical investigations have also been carried out; due to the complexity of the configuration, they are generally based on simplified assumptions that limit the validity domain of the obtained results. For instance, Mie theoretical model (Mie, 1908) only applies for one spherical or ellipsoidal scatter and assumes an incident plane wave (Van Der Baan, 2001). investigates and models the frequency variation of volume scattering induced by Gaussian distributed heterogeneities but in 1D, assuming plane waves, and focusing on transmission through the heterogeneous medium (rather than reception after propagation and scattering).

This paper proposes a method to statistically estimate the typical size of buried scatterers from WISDOM radargrams. The method takes advantage of the broad frequency bandwidth of WISDOM, but it can be applied to any ultra-wideband GPR. The proposed method is described in Section 2, which shows how numerical simulations are performed to generate realistic synthetic WISDOM data on heterogeneous subsurfaces. Section 3 focuses on the main results, namely how the typical size of the embedded heterogeneities can be estimated from the synthetic dataset and the validation of the method on experimental data acquired in a partially documented environment. Section 4 is dedicated to discussions about the robustness and limitations of the method. The last section is devoted to conclusions.

2. Method

The study of the volume scattering phenomenon is based on synthetic data representative of the experimental data that WISDOM would acquire on heterogeneous subsurfaces.

2.1. Generation of WISDOM synthetic data

The numerical simulations run to generate the synthetic data take into account both the characteristics of the WISDOM radar and a number of heterogenous 3D subsurface models that are described further in this section.

2.1.1. The WISDOM GPR

WISDOM is a dual-polarimetric ground penetrating radar designed to characterize the shallow subsurface of Mars along the Rosalind Franklin rover path. It will be operated during traverses before any drilling activity and provide high-resolution radargrams of the first meters below the surface. The mission drill is designed to dig down to 2 m and collect 3 cm–long core samples of subsurface material. The drill capacity served as guideline for WISDOM design. WISDOM will produce images of the subsurface down to a depth of 2–5 m with a vertical resolution of a few

centimeters, depending on the subsurface geoelectrical characteristics. It has three main objectives. First, to understand the 3-D geology and geologic evolution of the site in synergy with surface images acquired by other instruments, such as PanCam (Coates et al., 2017) and CLUPI (Josset et al., 2017). This analysis will be based on the buried structures revealed by WISDOM (stratigraphy, spatial heterogeneity …), and on the effective electrical properties of the detected units (interpreted in terms of physical and compositional properties). Second, WISDOM will investigate the local distribution and state of subsurface water. This includes the search for potential segregated bodies of ground ice and transient occurrence of liquid water/brine in the near-surface. Third, WISDOM will identify the safest and most promising scientific targets for subsurface sampling by the drill and provide an accurate estimate of the depth for the sample acquisition. After a drilling, WISDOM data products will be used to extrapolate in a 2-D (or 3-D depending on the Rover's path) map the compositional information provided along the vertical direction by the Ma_MISS infrared spectrometer (De Sanctis et al., 2017) located inside the drill (Altieri et al., 2023).

WISDOM is a step frequency radar operating on a broad frequency bandwidth B = 2.5 GHz in the UHF domain, from 0.5 GHz to 3 GHz, which corresponds in vacuum to wavelengths from 10 cm to 60 cm. For each sounding, a series of N = 1001 harmonic pulses (of duration $\tau = 1$ ms) with a frequency step of $\Delta f = \frac{B}{N-1} = 2.5$ MHz is generated and transmitted by the transmitting antenna. The N resulting electromagnetic waves propagate toward the surface and into the subsurface and are reflected/scattered by permittivity contrasts in the sounded volume. The portion of the waves that returns to the radar is eventually converted into a signal by the receiving antenna. Inside the receiver, for each frequency, the received signal is multiplied by the transmitted signal, low-pass filtered and sampled. The resulting voltage value is recorded. Therefore, WISDOM raw data for one sounding consists of a series of N values corresponding to the sounded environment's transfer function at each frequency. The processing applied to these frequency domain data is further explained in sections 2.2.1 and 2.2.2.

Moreover, WISDOM has polarimetric capabilities. The instrument is able to perform sounding in four polarization set-ups (Plettemeier et al., 2009): two co-polarized (HH, VV) and two cross-polarized (HV, VH). The cross-polarization is especially useful for the identification of rough interfaces or buried structures which depolarized the electric field.

2.1.2. Numerical simulations of WISDOM operations

The electromagnetic simulations used in this paper have been performed using a FDTD (Finite Difference Time Domain) code called TEMSI-FD and developed at XLIM (Limoges, France) by C. Guiffaut and A. Reineix (Besse, 2004; Le Gall, 2007). The FDTD method (Kunz and Luebbers, 1993; Taflove, 1995) is a numerical method widely used in electromagnetic simulations (Sullivan, 2013; Taflove et al., 2005), that computes the electromagnetic field within the considered volume as a function of space and propagation time. Compared to other methods operating in the frequency domain, which may run faster, it offers many advantages for our study. First, it is based on a rigorous formulation of Maxwell equations and solves directly the set of equations without any physical approximation. Secondly, it is a versatile method relatively easy to implement and the accuracy of the numerical scheme can be controlled by the time-steps and/or grid spacing. Working in the time domain is clearly an advantage since the actual waveform transmitted by the antenna (that has been experimentally characterized, see Hervé et al., 2020) can be used as the input signal and subsequent propagation and scattering of the waves can be followed in a straightforward manner. Lastly, it is a three-dimensional approach which makes it possible to take into account for sophisticated subsurface models, described by the values taken, at each cell of the considered volume, for the geoelectric parameters (namely the permeability, permittivity and conductivity) that drive the electromagnetic waves propagation. For the simulations, the permittivity and conductivity are combined in a complex parameter which is normalized by the permittivity of vacuum. In the following, for the sake of simplicity we refer to as "permittivity" ε the real part of the complex relative permittivity and ε'' the absolute value of its imaginary part, which is responsible for electrical losses. In the frame of the work presented in this paper only non-magnetic (i.e. with a permeability value equal to μ_0) and non-dispersive (ε and ε'' are not frequency dependant) materials are considered.

The whole computational volume is divided in 3-D cells (Yee, 1966), each cell being characterized by a set of ε and ε'' values. Doing so, sophisticated subsurface structures can be modelled down to the scale of the spatial mesh with no increase of the computational and memory resources. To obtain reliable simulated data, the size of the FDTD cells must be small enough to correctly capture the wave propagation through space and avoid numerical dispersion. The mesh grid spacing is commonly set to a value smaller than one tenth of the wavelength in the medium (Luebbers et al., 1993). In the case of WISDOM, this translates into cell size of typically less or equal to 5 mm. TEMSI-FD includes suitably absorbing boundary conditions with Perfectly Matched Layers (PML) (Berenger, 1994), to eliminate the parasitic reflections that occur on the walls of the computational volume. As a consequence, a part of the electromagnetic waves propagating in the vicinity of the volume's edges is lost in the PML. It is therefore essential to ensure that the calculation volume is large enough to minimize this effect. According to the radargram of Fig. 2e obtained on homogeneous layers, the first sounding not impacted by this boundary effect is 50 cm away from the vertical walls of the box. The minimal horizontal dimensions of the computational volume needed to correctly simulate one sounding are 1 m for the horizontal axes. The computational volume displayed in Figs. 1 and 2a ($3 \times 1 \times 1.5$ m^3) is long enough to allow the horizontal displacement of the radar needed to build a radargram.

Modeling WISDOM operations in TEMSI-FD requires to accurately model its Vivaldi antennas. The physical WISDOM antennas radiate toward the surface but are not very directive. Their radiation pattern has a 30° large main beam and side-lobes (Ciarletti et al., 2011). The WISDOM antennas are modelled to mimic these characteristics. Emission and reception antennas are represented by oblique wires (Guiffaut et al., 2012) derived from Holland wires (Holland and Simpson, 1981) following accurately the edges of the slot of the Vivaldi antennas where

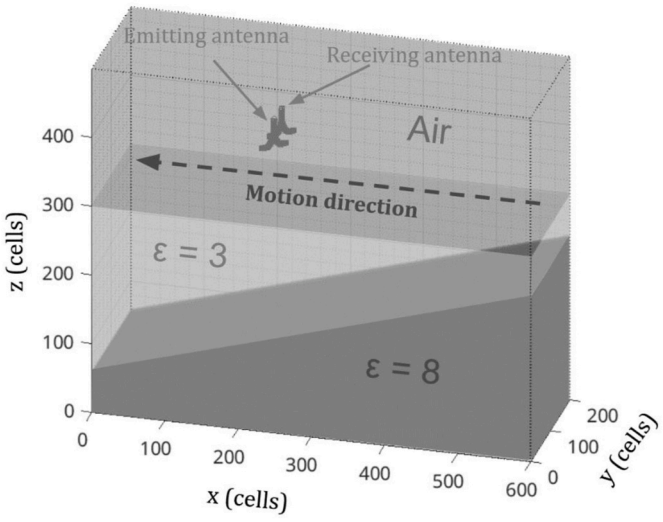

Fig. 1. Example of TEMSI-FD generated synthetic volume. The modelled WISDOM antennas are in red; they are located in the air (relative permittivity of 1), 38 cm above the surface and oriented at 45° to the motion direction, as on the Rosalind Franklin rover. The spatial axes x, y and z are expressed in cells; one cell is $5 \times 5 \times 5$ mm^3. The total simulated subsurface is $3 \times 1 \times 1.5$ m^3. The subsurface is composed of two homogeneous layers, the interface is a steep slope. The upper layer relative permittivity is 3 and the lower one is 8.

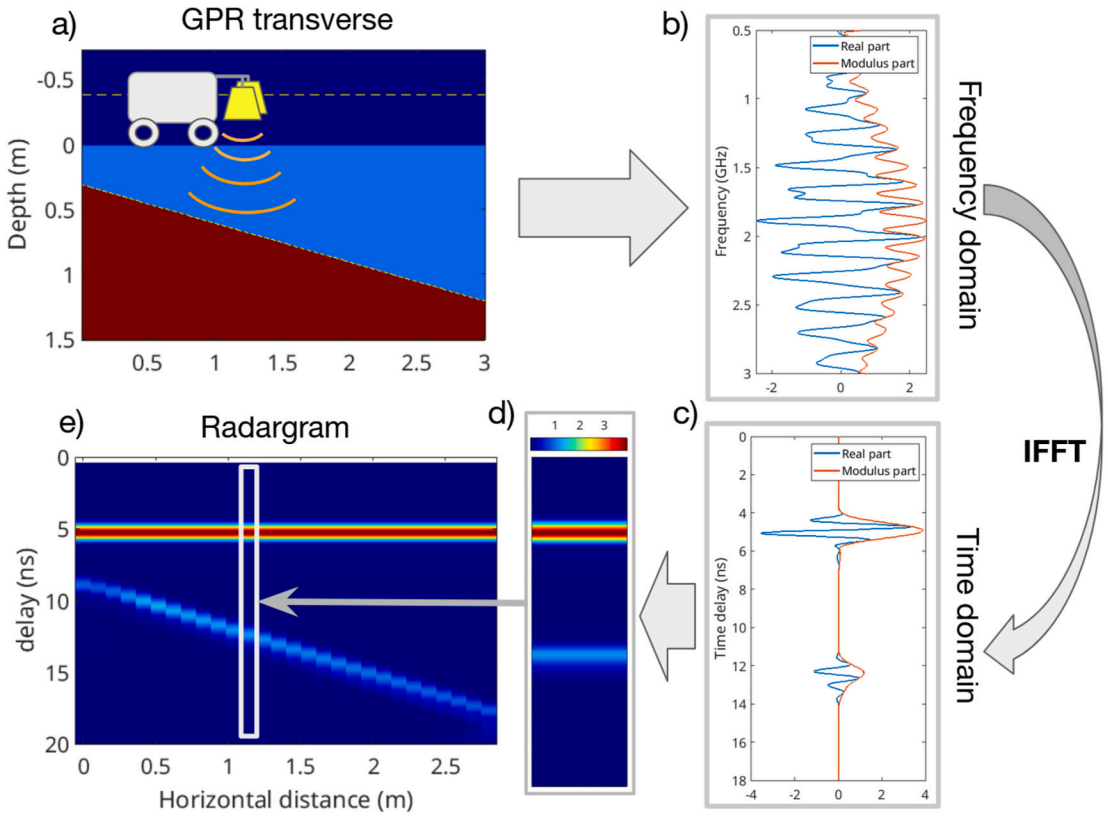

Fig. 2. From single sounding to radargram. (a) Slice of the simulated GPR traverse illustrated in Fig. 1; soundings performed every 10 cm. (b) Frequency spectrum of one single sounding. (c) Temporal spectrum (A-scan) after Inverse Fast Fourier transform of the frequency spectrum. We observe 2 echoes from top to bottom; the ground echo (~5 ns) and the buried interface echo (~12.5 ns). (d) Color scale displays the amplitude of the temporal spectrum in arbitrary units. (e) Side by side combination of A-scans provides a radargram. (For interpretation of the references to color in this figure legend, the reader is referred to the Web version of this article.)

current is concentrated. A resistive profile has been added to reduce reflections at the tips of the antennas (Wu and King, 1965). The emission antenna is fed by a sine-Gaussian model of the WISDOM time-domain equivalent impulse, experimentally determined by (Hervé, 2018). The simulation output is the signal measured by the reception antenna. As on the Rosalind Franklin rover, the distance between the emission and reception antennas is about 20 cm and both antennas are in the air, 38 cm above the modelled ground. Due to space constraints onboard, the antennas are also 45° tilted with respect to the motion direction of the rover (see Fig. 1).

TEMSI-FD also provides adequate fractal models to simulate non-homogeneous environments that will be presented in details in section 2.1.3.

The WISDOM GPR operates in the frequency-domain (Fig. 2b), but the interpretation of the data is most commonly performed in time domain (Fig. 2c) after an Inverse Fourier Transform. A sounding in time-domain, usually referred to as a "A-scan" (Fig. 2c), displays the time delays and amplitudes of echoes from reflectors within the volume illuminated by the antenna radiation pattern in a nadir-looking viewing geometry. A GPR traverse (Fig. 2a) consists in performing equal-step separated soundings along a path at the surface. The combination of all A-scans acquired during the GPR traverse provides a 2-D "map" of the subsurface called "radargram" (Fig. 2e) and also known as "B-scan". Because the antenna radiation pattern illuminates a broad volume in 3-D, a radargram is actually a projection of the sounded volume on a plane.

2.1.3. *Generation of realistic heterogenous subsurface models*

In order to statistically study the effect of realistic heterogeneities on simulated WISDOM data, we chose to model the variability of the permittivity value in the subsurface by a band-limited fractal process. The TEMSI-FD code allows to generate synthetic subsurfaces with embedded heterogeneities of fractal properties with the diamond-square splitting technique (Miller, 1986). The heterogeneity is modelled by spatial variations of ε and/or ε'' values. The diamond-square algorithm is usually applied to generate fractal terrains for instance for scenery generator in computing graphics.

In two dimensions, the algorithm begins with a 2-D square array of width and height $2^N + 1$, where N is the total number of iterations. The four corner points of the array must first be set to initial values. The three following steps are repeated until all array values have been assigned (thus N times):

(i) The diamond phase: For each square in the array, the midpoint of that square is set to be the average of the four corner points plus a random value.
(ii) The square phase: For each diamond in the array, the midpoint of that diamond is set to be the average of the four corner points plus a random value.
(iii) The spatial step (or width of the squares in the array) is divided by 2.

At each iteration, the magnitude of the random value decreases to maintain consistency in the texture of the terrain.

In TEMSI-FD, this algorithm is applied on 3-D array to generate volumes of fractal properties. Our study relies on these fractal heterogeneous subsurfaces. Fig. 3a, b and 3c display three of them as examples. The values set by the algorithm in the volume are permittivity values (or electrical conductivity values) (see color scale on Fig. 3). The distribution of permittivity values in the synthetic subsurface can be either

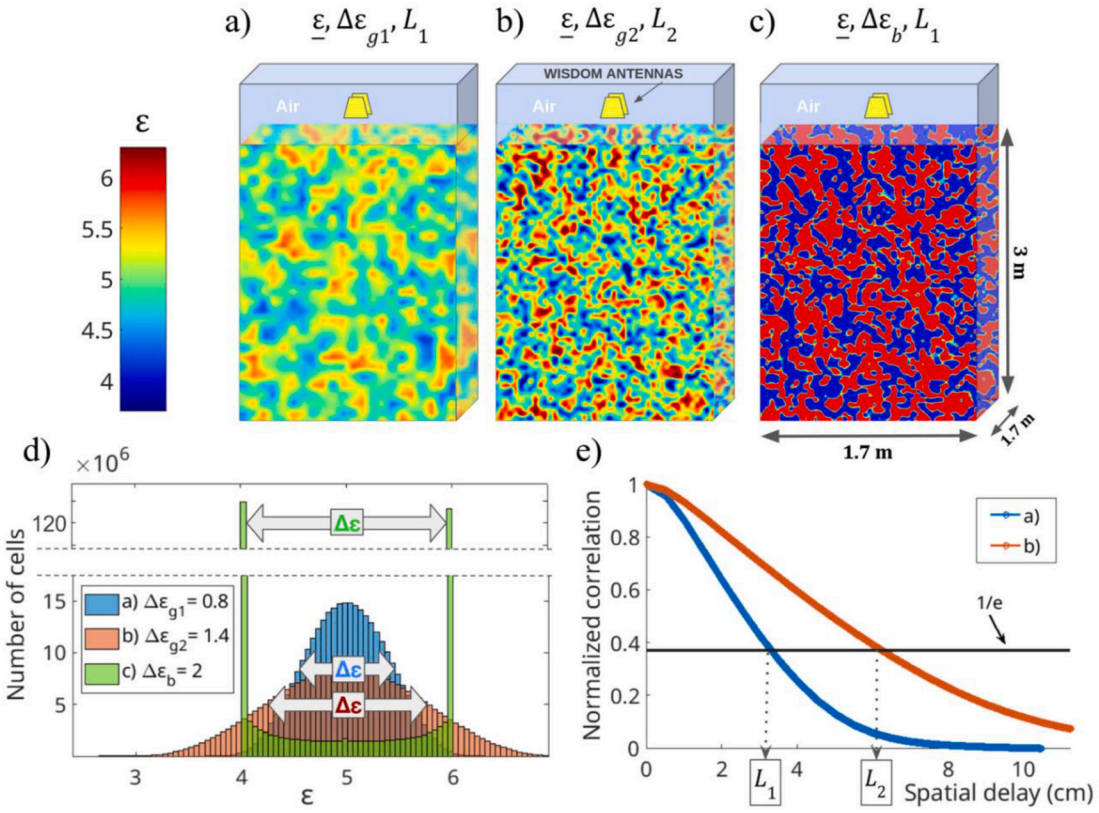

Fig. 3. 3-D examples of simulated volumes with fractal heterogeneous subsurfaces and determination of their physical parameters. (a) Gaussian distribution subsurface characterized by "large" typical size of heterogeneities and "small" permittivity contrasts. (b) Gaussian distribution subsurface characterized by "small" typical size of heterogeneities and "strong" permittivity contrasts. (c) Bi-modal distribution subsurface characterized by "small" typical size of heterogeneities. (d) Permittivity values distribution and associated $\Delta\varepsilon_{g1}$, $\Delta\varepsilon_{g2}$ and $\Delta\varepsilon_b$. (e) Correlation lengths L_1 and L_2 of heterogeneities determined from the correlation curve. L is given by the intersection of the correlation curve with the grey horizontal line at 1/e by convention (see dotted arrows).

gaussian (Fig. 3a and b) or bi-modal (Fig. 3c–ie., half of the cells have the same permittivity value and the other half have another permittivity value).

In the gaussian case, the fractal heterogeneous features generated with TEMSI-FD consist of smooth and continuous variations of the permittivity value which has a gaussian distribution in the generated volume (Fig. 3d). In the bi-modal case, there is only two possible values of permittivity, which results in sharp permittivity discontinuities at the interfaces between fractal heterogeneous features (Fig. 3c). Such synthetic heterogeneous volumes can be described by a number of physical parameters, which will be presented in detail in the following section.

TEMSI-FD also allows to generate different stochastic realizations with the same physical parameter values. Their statistical physical properties are the same, but the algorithm is initialized by an integer value that ensures that the very same random generation can be obtained several times when needed, which is useful to modify only one physical parameter at a time and compare results (see examples of Fig. 3b and c). For these specific simulations involving heterogeneous subsurface models, the dimensions of the computational volume have been studied. (i) Because of volume scattering, a larger distance to the edge of the box is required. A series of tests led to the conclusion that a distance of 80 cm is needed (rather than the 50 cm suitable for homogenous media). (ii) the WISDOM GPR has been multiple times tested on the field (e.g., Hervé, 2018; Oudart, 2021); it is expected to detect reflectors buried at a depth of 2–3 m (Dorizon et al., 2014), exceptionally >5 m in especially low-loss (mostly icy) environments (Dorizon et al., 2016). To account for this reality, we chose a depth of 3 m for our synthetic media. Hence, to simulate a single sounding, we decide to consider a box size of (1.7 m × 1.7 m × 3 m) which is large enough as long as the antennas are located at the center of the box.

For a box size set to (1.7 m × 1.7 m × 3 m) with a cell size of 5 mm × 5 mm × 5 mm, a time step of $4{\cdot}10^{-3}$ ns, one sounding simulation requires about 2 h of computation for an 8 cores parallelized calculation on an Intel Xeon E5-4627 v2 Processor. The computational time is independent of the physical parameters of the medium.

2.1.4. *Physical descriptors of the generated heterogeneous subsurfaces*

A given subsurface can be characterized by a number of physical parameters (composition, density, porosity, level and type of homogeneity, size of inclusions, etc.). Yet, GPR only sense spatial variations in the value of permittivity in a given medium (provided it is a non-magnetic medium as assumed for this work). These changes cause reflections and/or scattering and absorption of the transmitted waves that are eventually received by the receiving antennas. Thus, the relevant parameters for our study, that will be used in the TEMSI-FD code to generate a heterogeneous medium are.

(i) the mean permittivity $\underline{\varepsilon}$ of the subsurface
(ii) the contrast of permittivity $\Delta\varepsilon$.
(iii) the typical size of the scatterers L

The mean permittivity $\underline{\varepsilon}$ of the subsurface

For sake of simplicity and as a starting point, the imaginary part of the permittivity is assumed to be null (i.e., $\varepsilon'' = 0$). In other words, the media are considered as loss-less (the impact of electrical losses will be analyzed later in section 4.3).

Furthermore, we highlight that the relevant physical quantity that affects EM waves propagating within a heterogeneous subsurface in terms of amplitude and wavelength is not the permittivity but the square root of the permittivity. Indeed, the wave velocity v is proportional to $\frac{1}{\sqrt{\varepsilon}}$

as well as the wavelength in a medium $\lambda \propto \frac{1}{\sqrt{\varepsilon}}$. Furthermore, the transmissivity and reflectivity Fresnel coefficients for an incident plane nadir-looking wave at a horizontal smooth interface between two semi-infinite media of permittivity ε_1 and ε_2 are also functions of the permittivity square root: $T_{Fresnel} \propto \left(\frac{\sqrt{\varepsilon_1}}{\sqrt{\varepsilon_1}+\sqrt{\varepsilon_2}}\right)^2$ and $R_{Fresnel} \propto \left(\frac{\sqrt{\varepsilon_1}-\sqrt{\varepsilon_2}}{\sqrt{\varepsilon_1}+\sqrt{\varepsilon_2}}\right)^2$.

We therefore define the mean permittivity and contrast of permittivity from the distribution of the square root of the permittivity values.

For a given synthetic numerical volume (built with N cells), for any type of permittivity distribution (gaussian or bi-modal), the mean effective permittivity is defined as $\underline{\varepsilon} = \left[\frac{1}{N}\sum_{i=1}^{N}\sqrt{\varepsilon_i}\right]^2$. This parameter is referred to as an "effective permittivity" since, in a heterogeneous medium, the subsurface consists in a mixture of materials of different electrical properties.

The contrast of permittivity $\Delta\varepsilon$.

The parameter describing the dispersion of the square root of permittivity values around the square root value of the effective permittivity is the standard deviation of the distribution of the square root of the permittivity values $std\left(\sqrt{\varepsilon}\right) = \sqrt{\frac{1}{N}\sum_{i=1}^{N}\left(\sqrt{\underline{\varepsilon}} - \sqrt{\varepsilon_i}\right)^2}$.

For a bi-modal permittivity distribution characterized by two values ε_+ and ε_-, the two parameters defined above give $\underline{\varepsilon} = \left[\frac{\sqrt{\varepsilon_+}+\sqrt{\varepsilon_-}}{2}\right]^2$ and $std\left(\sqrt{\varepsilon}\right) = \frac{1}{2}\left(\sqrt{\varepsilon_+} - \sqrt{\varepsilon_-}\right)$.

We choose to define the contrast of permittivity as $\varepsilon_b = \varepsilon_+ - \varepsilon_-$, which corresponds to

$$\Delta\varepsilon_b = 4\sqrt{\underline{\varepsilon}} \times \left(\sqrt{\varepsilon_+} - \sqrt{\varepsilon_-}\right).$$

For a gaussian distribution of permittivity, we choose the same definition to define the permittivity contrast as $\Delta\varepsilon_g = 4\sqrt{\underline{\varepsilon}} \times std\left(\sqrt{\varepsilon}\right)$.

The typical size of the scatterers L.

We define the typical size L of the heterogeneities from the 3-D auto-correlation of the permittivity values in the volume. More specifically, to properly estimate the L value, we retrieve the correlation length value as the spatial shift for which the auto-correlation function has decreased by a factor $\frac{1}{e}$ (0.37, Fig. 3e).

In this work, we demonstrate that the WISDOM data acquired on a heterogeneous terrain can be used to retrieve the value of one or several of these 3 physical parameters. We therefore below explore the effects of these 3 parameters on the returned signal.

2.2. Impact of the size of heterogeneities on the radar data

The heterogeneous 3-D subsurfaces generated as explained above are used to produce simulated GPR data, which are then the basis for the proposed method able to retrieve the typical size of the heterogeneities.

2.2.1. Pre-processing of the GPR data

When performing a sounding, WISDOM transmits and receives a series of 1001 harmonic signals of frequencies f ranging between $f_{min} = 0.5$ GHz and $f_{max} = 3$ GHz and separated by a constant frequency step of $\Delta f = 2.5$ MHz. Only the real part of the returned signal is recorded by the instrument, and the imaginary part is reconstructed by a Hilbert transform. Fig. 4a displays a typical WISDOM spectrum.

The data processing pipeline developed for WISDOM is described in details in (Hervé et al., 2020). Here we only describe the most relevant processing step mandatory for this study: the signal whitening. Indeed, the end-to-end frequency response of the instrument (including transmission and reception channels) is not constant over the whole WISDOM bandwidth (Fig. 4b). As a consequence, in order to estimate correctly the frequency dependency of the subsurface response, a "signal whitening" or "spectrum compensation" has to be performed prior to any analysis. This consists in dividing the measured spectrum by the instrument transfer function which can be obtained from the WISDOM spectrum of an echo on a perfect reflector (Fig. 4b). We usually use a metallic plate located at the same distance to the antenna as the ground as a perfect reflector, both for synthetic data and experimental data (Fig. 5). This processing step ensures that any frequency-dependent phenomena observed in the radar data are caused by the propagation medium.

2.2.2. Analysis of the radargrams by sub-bands in the frequency domain

Fig. 2 shows an example of synthetic radargram obtained for a subsurface composed of two homogeneous media separated by a clear interface (i.e., a discontinuity in permittivity). The resulting radargram (Fig. 2e) is an image of the subsurface projected on the plane vertical to the radar (Fig. 2a). The upper layer permittivity can be inferred by comparing the surface echo intensity to the metallic plate echo intensity (Dorizon et al., 2016). Thanks to the derived permittivity value, the depth and slope of the buried interface can be estimated.

In contrast, when soundings are performed over a heterogeneous

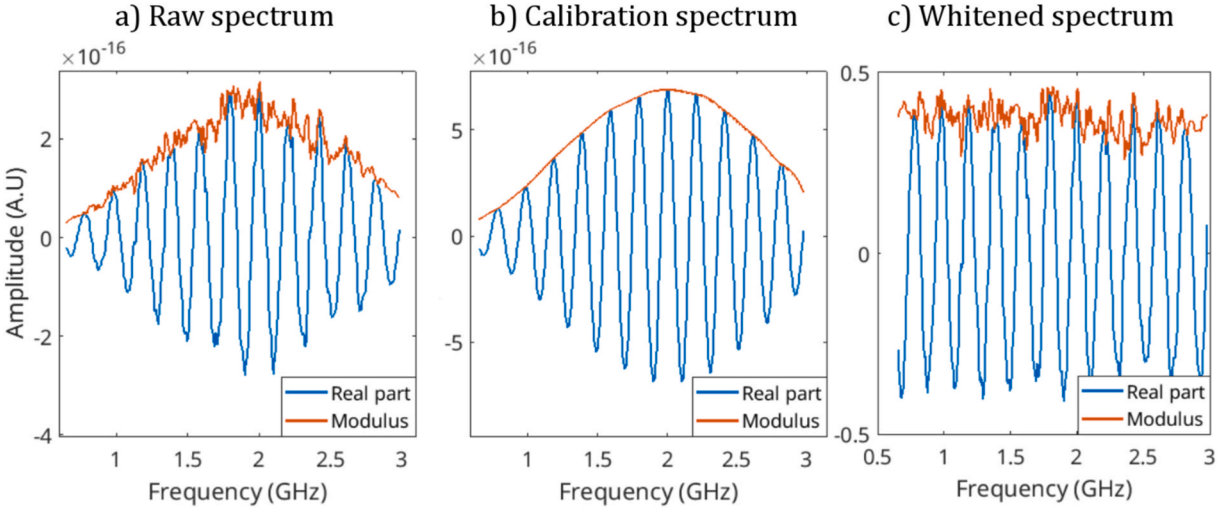

Fig. 4. Whitening process in the frequency domain. a) Raw spectrum directly measured by WISDOM on Fig. 3b medium. The surface is smooth and horizontal. Note that this spectrum includes the surface echo plus the volume backscatter by the heterogeneous subsurface. b) Calibration spectrum obtained by performing a synthetic sounding on a perfect metallic plate. c) Compensation of the raw spectrum by the envelope of the calibration spectrum to obtain the whitened spectrum.

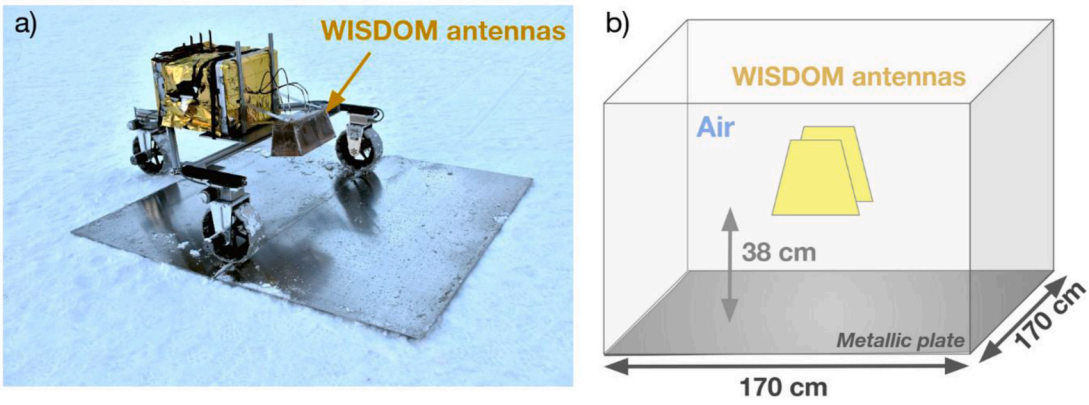

Fig. 5. (a) Example of calibration performed in 2002 on a metallic plate during a field campaign on Svalbard, Arctic Norway. (b) TEMSI-FD calibration simulation. The antenna height above the ground (38 cm) is the same as on the Rosalind Franklin rover.

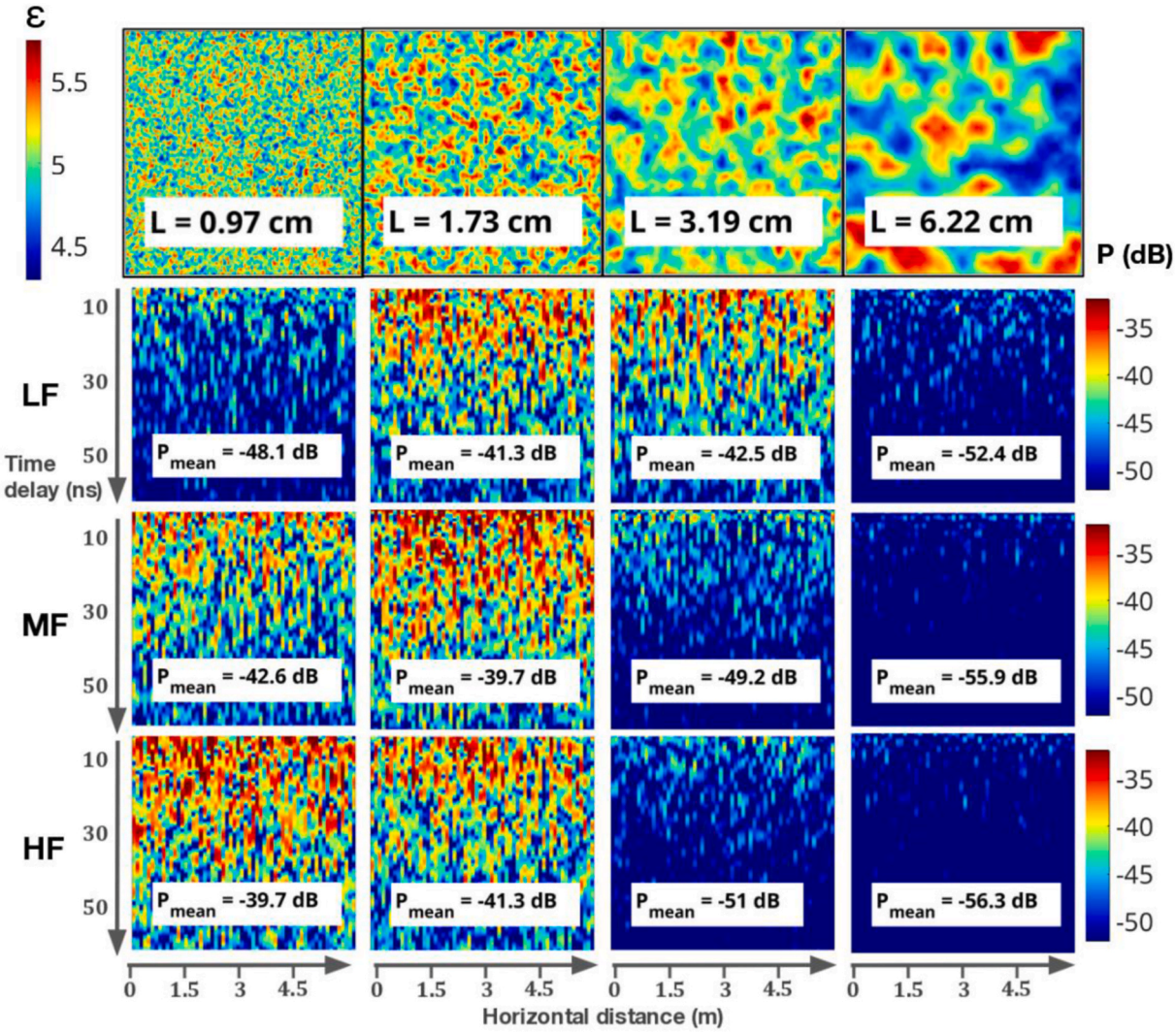

Fig. 6. Four synthetic subsurfaces with increasing sizes of heterogeneities (upper figures) and the corresponding radargrams below. $\underline{\varepsilon} = 5$ and $\Delta\varepsilon = 0.5$ are the same for all four media. The radargrams are built from different frequency windows in the frequency domain of WISDOM. From top to bottom: Low Frequency (LF) is the window [0.5–1.33] GHz, Medium Frequency (MF) is [1.33–2.16] GHz and High Frequency is [2.16–3] GHz. The same color scale is used for all radargrams. P_{mean} is the normalized volume backscatter intensity averaged on each radargram (mean computed on the range 10–50 ns). (For interpretation of the references to color in this figure legend, the reader is referred to the Web version of this article.)

medium with spatial variations of permittivity at small scales (typically $\langle 10\ \text{cm} <$ for WISDOM wavelengths, Fig. 6 top panel), the resulting radargram shows no recognizable features (Fig. 6 three lower panels). Waves are scattered by these heterogeneities and signals arrive at various time delays, from various directions and with various intensities which appear randomly spread over the radargrams.

However, these signals contain information: they result from multiples reflections/scattering on a statistical number of small scatterers. Because the efficiency of such reflections/scattering depends on the propagating wavelength with respect to the size of the scatterers, such dependence should appear when investigating WISDOM radargrams on restrained bands (or sub-bands) of the initial wide frequency bandwidth as illustrated by Fig. 6.

The three lower panels of Fig. 6 show, for different frequency sub-bands, the synthetic radargrams obtained over four different heterogeneous subsurfaces with variable typical size of heterogeneities L but constant $(\Delta\varepsilon, \underline{\varepsilon})$. The WISDOM frequency domain has been subdivided into 3 frequency windows of equal width: LF (Low Frequency) between 0.5 and 1.33 GHz, MF (Medium Frequency) between 1.33 and 2.16 GHz and HF (High Frequency) 2.16 and 3 GHz.

At first sight, the resulting radargrams significantly differ from a frequency window to another.

The smallest heterogeneities (first column in Fig. 6) generate significantly more backscattered signal at HF than at LF. With increasing L, the maximum backscattering is reached at the lowest frequencies. For L = 6.22 cm, there is almost no volume scattering anymore, but only early echoes due to near-surface reflections.

To allow a quantitative study of this frequency dependent phenomenon, we introduce P_{mean} (expressed in dB), the normalized backscattered signal intensity. More specifically, $P_{mean} = 10 \times \log \frac{1}{M} \sum_{s=1}^{M} \frac{\overline{I_{s|10-50|ns}}}{I_{DC}}$ where I_s is the mean signal intensity computed over M soundings and over the time range [10–50] ns (10 ns being the earliest delay after surface echo and 50 ns the average delay to reach the 3-m deep bottom of the computational volume for a mean effective permittivity value of 5). I_s is normalized by the direct coupling signal intensity I_{DC}, which is the strongest signal in WISDOM radargram. We highlight that the surface echo is excluded from this study, hence P_{mean} is exclusively computed on backscattered signal and is therefore a relevant metric for quantitative comparison.

In nominal configuration, the effective dynamic range of WISDOM is 66 dB (Hervé, 2018). Thus, we can consider that any signal whose power exceeds −66 dB with respect to the direct coupling power is above the noise level and therefore significant and actually due to volume scattering. Despite the relatively low contrast in permittivity value $\Delta\varepsilon = 0.5$ in Fig. 6 (upper panel), P_{mean} is ranging between −40 dB and −56 dB, which remains significantly above the −66 dB threshold.

The frequency dependent behavior observed on the four simulated radargrams in Fig. 6 suggests that it is possible to use of the ultra-wide bandwidth of the GPR to perform a quantitative analysis and recover the typical size of subsurface heterogeneities.

2.2.3. *Quantitative analysis of the synthetic data in the frequency domain*

Fig. 6 illustrates the sensitivity of WISDOM data to the size of the heterogeneity parameter using only 3 frequency sub-bands, we propose to go further by using a sliding sub-frequency window of a given width SW_{BW} to sweep the whole instrument bandwidth. For each of the N positions of the sliding window, we compute the mean volume backscatter intensity P_{mean} as explained in section 2.2.2.

In addition, to exhibit a possible general trend in the relationship between volume backscattering and frequency, more than a single sounding on a single synthetic heterogeneous subsurface must be simulated. We thus achieve a number (typically 60) of different stochastic realizations with the same subsurface physical properties $(L, \Delta\varepsilon, \underline{\varepsilon})$ (Fig. 7a). Furthermore, to guarantee a set of uncorrelated GPR data, only one sounding is performed on each synthetic medium as illustrated by Fig. 7a. From these stochastic realizations, we then perform ensemble averages to obtain a mean value of the backscatter

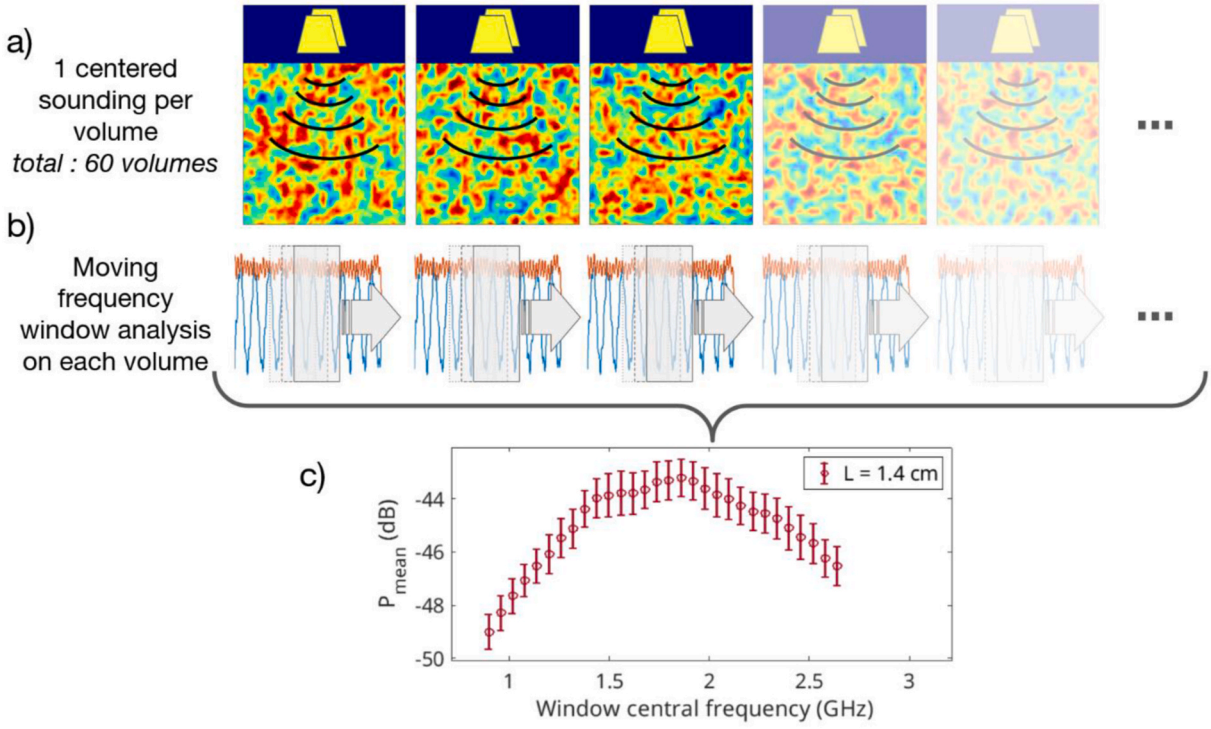

Fig. 7. (a) One single sounding is performed at the center of each synthetic volume. The operation is repeated on 60 independently generated volumes having the same physical parameter values $L = 1.4$ cm, $\Delta\varepsilon_g = 0.3, \underline{\varepsilon} = 5$. (b) The sliding window process is conducted on each sounding. The window width is here 600 MHz and the frequency step is 90 MHz. (c) P_{mean} as a function of the center frequency for each window and its associated standard deviation computed over the 60 independent soundings.

power and its statistical variability.

Fig. 7a and b illustrate the method. Fig. 7c represents, for $N = 20$, P_{mean} as a function of $[f_i]_{i\in[1,N]}$ where f_i is the central frequency of the i-th sliding frequency window. It clearly shows, for the example considered (i.e., $L = 1.4$ cm, $\Delta\varepsilon_g = 0.3, \underline{\varepsilon} = 5$), the dependency of backscattering by heterogeneities with respect to frequency. For each of these N frequency bands, the mean and the standard deviation of P_{mean} are computed over a set of 60 independent soundings as shown in Fig. 7.

For this study to be statistically relevant, the computational box must also contain a large number of scatterers. This is the case as for the largest investigated size of heterogeneities L = 6 cm, the considered synthetic subsurface (1.7 m × 1.7 m × 3 m) contains more than ten thousand scatterers.

As anticipated and illustrated by Fig. 7c, all WISDOM frequencies are not equally backscattered. For a L value of 1.4 cm, a maximum emerges around 1.8 GHz.

Additional simulations show that the position of this maximum changes with the value of L and that a more relevant quantity than frequency or wavelength to investigate P_{mean} variations is the ratio $\frac{L}{\lambda}$ where $\lambda = \frac{c}{f\sqrt{\underline{\varepsilon}}}$ is the wavelength in the subsurface of mean effective permittivity $\underline{\varepsilon}$.

Examples illustrating, for a given permittivity distribution but with different L values, the frequency dependence of P_{mean} are presented in Fig. 8 as a function of kL where $k = 2\pi/\lambda$ is the wave number in the medium. Fig. 8a corresponds to a case of Gaussian distribution and Fig. 8b to a case of bimodal distribution. Both curves show a clear maximum occurring for a kL value close to 1.25, followed by oscillations for larger kL values. They bear similarities with the curve obtained for the Mie scattering radar cross section of a sphere (Mie, 1908), which is consistent with the fact that the explored range of kL values actually corresponds to the Mie scattering region for $kL > 0.7$ and to the Rayleigh region for $kL < 0.7$.

The global maximum observed on Fig. 8 is actually close to the first Mie resonance, which arises at $kr = 1$ for a perfect electromagnetic conductor sphere of radius r. Theoretical computation using analytical functions for a dielectric sphere (Bohren and Huffman, 1983) of permittivity 5.5 in a medium of permittivity 5 (a similar permittivity contrast and mean effective permittivity as in Fig. 8) leads to a first resonance maximum at $kr = 1.36$.

The results obtained in this paper exclusively rely on the position of the global maximum observed for P_{mean}.

3. Results

The method described in the previous section is used to obtain a quantitative relationship to recover the size of heterogeneities using radargrams.

3.1. Relationship between the position of the backscatter maximum and the size of the heterogeneities

To obtain a relationship useable for relevant configurations, we generated synthetic radar data for a variety of subsurface models exploring a large parameter space for $(L, \Delta\varepsilon, \underline{\varepsilon})$:

- $\underline{\varepsilon}$ varies from 1.2 to 9, with most of the simulations at $\underline{\varepsilon} = 5$.
- $\Delta\varepsilon$ varies from 0.01 to 4 (but in a majority of cases between 0.3 and 2).
- L varies from 0.7 cm to 6 cm.

As mentioned previously, we also consider two very different distributions of permittivity values to account for a variety of configurations in natural environments: the gaussian distribution representing smooth variations in permittivity and the bi-modal distribution representing small inclusions in a homogeneous matrix. All simulations run show a shape of the scattering curve around its maximum similar to those presented in Fig. 8, regardless of the mean effective permittivity $\underline{\varepsilon}$ and the permittivity contrast $\Delta\varepsilon$ (within the explored range).

We therefore chose to establish the position of the maximum by a method based on the whole set of simulated data i.e., obtained for both types of distributions and all values of $(L, \Delta\varepsilon, \underline{\varepsilon})$. Of prime importance, this implies that when analyzing experimental data in an unknown environment, determining the size of the scatterers does not require *a priori* knowledge of the geoelectrical properties of the materials in the subsurface (values and distribution).

Fig. 9 represents the bivariate histogram of P_{mean} and kL for all simulated data. We chose to fit the scatterplot of P_{mean} as a function of the dimensionless parameter kL around its global maximum (considering the kL values ranging between 0.45 and 2.1) by a third-degree polynomial (a second-degree polynomial cannot fit the left-right

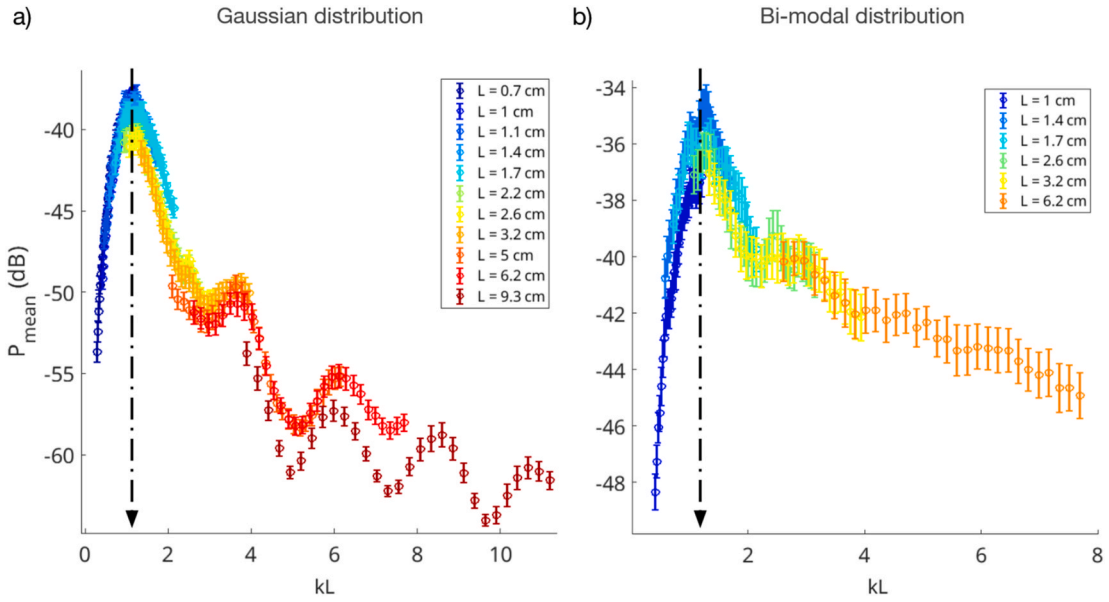

Fig. 8. P_{mean} as a function of kL for different values of L obtained for heterogenous subsurfaces with (a) a gaussian permittivity distribution with parameters $(\Delta\varepsilon_g = 0.55\ ; \underline{\varepsilon} = 5)$ and (b) a bi-modal permittivity distribution with parameters $(\Delta\varepsilon_b = 1, \underline{\varepsilon} = 5)$.

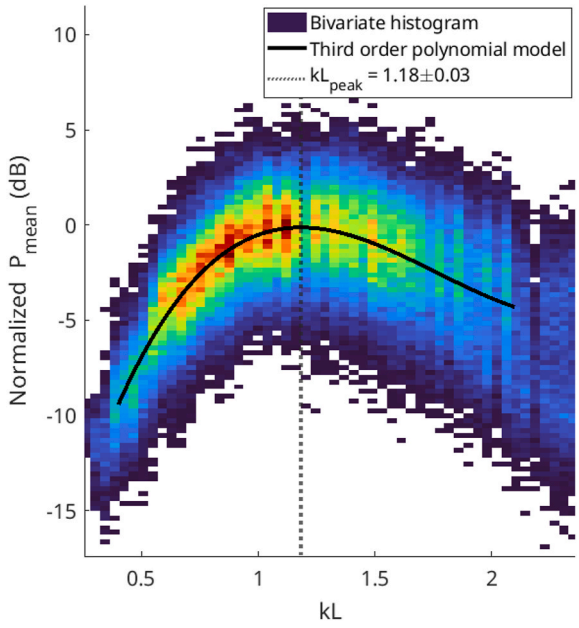

Fig. 9. Bivariate histogram of P_{mean} and kL. The best fit by a third-degree polynomial fit is shown as a black continuous line. The position of the maximum obtained using the fit is represented by a dotted vertical line.

asymmetry around the maximum) using the least square method. We then derived from the best-fit polynomial the position of the global maximum backscatter.

The associated uncertainties are obtained by a Monte Carlo method. This results in $k_{peak}L = 1.18 \pm 0.03$, which translates in $\frac{\lambda_{peak}}{L} = 5.3 \pm 0.2$. The position of the global maximum therefore offers a direct mean to estimate the typical size L of buried heterogeneities. The relative error on the value 5.3 is less than 4%, which leads to an error smaller than 1 mm in the retrieval of a scatterer size of $L = 2.5$ cm.

This error is small compared to the many other potential sources of errors when applying this method in the field (mean permittivity estimate, mixture of different sizes of scatterers, instrumental artefacts having a frequency dependence …).

3.2. Validation on experimental data

Relying on numerical simulations, we explored the effect of heterogeneities on the backscatter signal for a large variety of media with full control on physical parameters. However, measurements in natural environments are contaminated by different sources of noise and artefacts which can complicate the analysis. Therefore, the method proposed in this paper has to be tested on experimental data acquired on natural but documented environments.

3.2.1. Description of the experimental environment

To test the ability of the proposed method to estimate L, we selected media where the typical size of the embedded scatterers can be measured and where the standard deviation of the typical size distri-

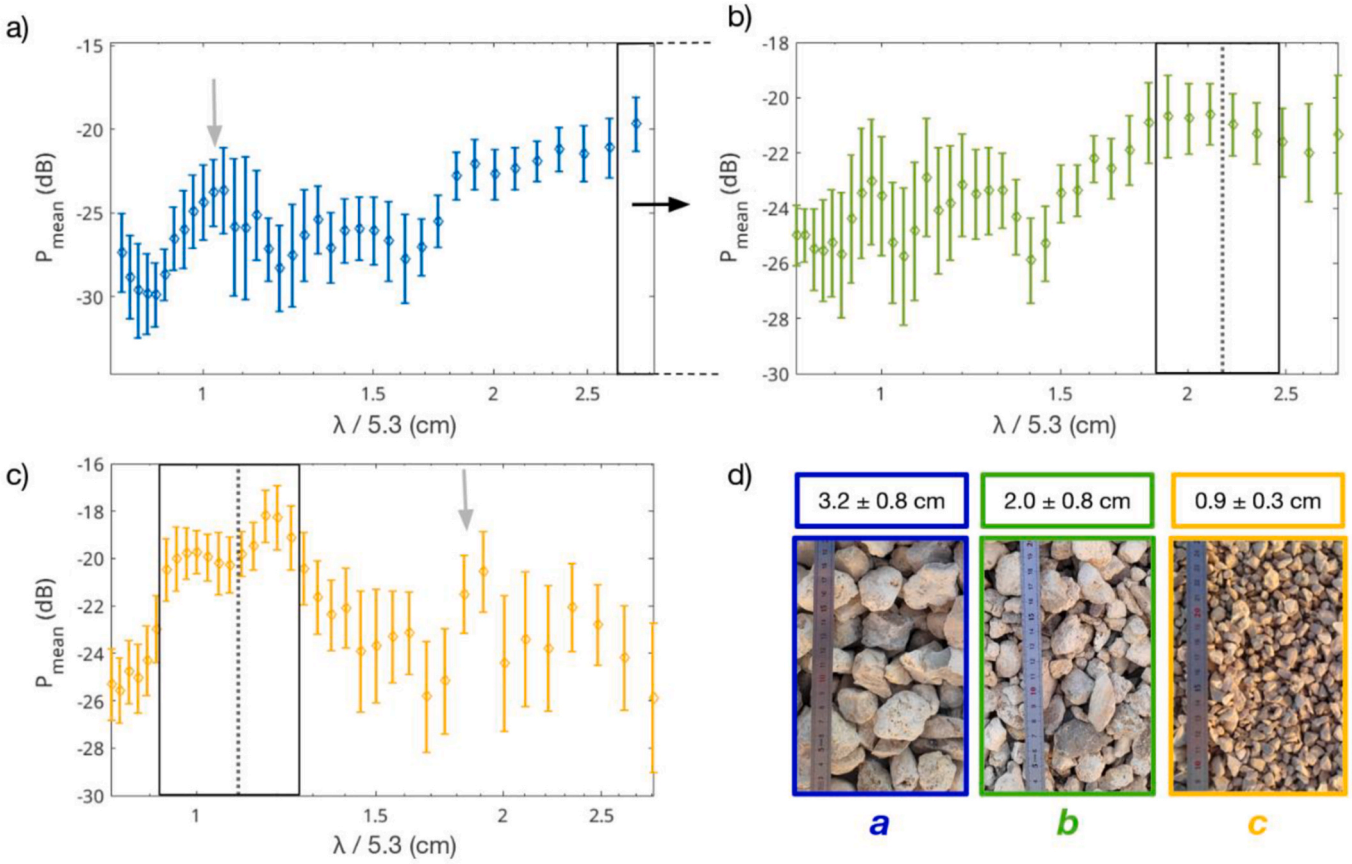

Fig. 10. (a), (b) and (c) display P_{mean} as a function of $\frac{\lambda}{5.3}$ from the soundings of three gravel piles with different granulometry as shown with a scale in (d). The grey dotted vertical lines represent the position of the maximum of P_{mean}, namely $L = \frac{\lambda_{peak}}{5.3}$ as determined by the third-degree polynomial fitting. The black rectangles indicate, for each pile, the error range on the estimate of L from the polynomial fitting. The wavelength λ propagating in the piles is calculated for a permittivity $\varepsilon_{pile} = 6$.

bution remains smaller than the typical size value itself. More specifically, we performed a series of measurements with WISDOM on three gravel piles near a construction site. Each pile is composed of gravels with a similar composition but a different granulometry. This provides a set of three scattering media composed of the same material but with three different typical sizes of scatterers (Fig. 10d).

The respective size distributions of the sounded media were characterized by measuring the size of hundreds of gravels randomly collected in each pile. The mean estimated sizes are 3.2 cm (gravel *a*, blue), 2.0 cm (gravel *b*, green) and 0.9 cm (gravel *c*, yellow), which is compatible with the scatterer size range that can be identified from WISDOM observations (see section 4.1). As shown by Fig. 10d, the grains have no specific shape; they can be angular or rounded. The voids between the gravels are mostly filled with air ($\varepsilon = 1$) and sand ($\varepsilon = 3-4$), which, at the epoch of the field test, was not totally dry in the interior of the piles. The permittivity of the mixture is not well constrained, we assume that the pile effective permittivity ranges from $\underline{\varepsilon}_{pile} = 6$ (Feitor et al., 2011; Salat and Junge, 2010) in the "dry limit", and up to $\underline{\varepsilon}_{pile} = 10$ (Arcone et al., 2003) in the moist case. Due to the high permittivity value and perhaps the humidity, the signal likely did not penetrate more than a few tens of centimeters. The permittivity distribution of the piles can be regarded as bi-modal somewhat similar as those simulated under TEMSI-FD except that gravels are not fractal in shape. Since the permittivity of the investigated media is not well known, we here only focus on testing our ability to retrieve the typical size of the gravels.

3.2.2. Analysis of the experimental data

The analysis (section 3.1) of a large synthetic data set demonstrated that a good estimate of the typical size of heterogeneities is $L = \frac{\lambda_{peak}}{5.3}$ where λ_{peak} is the wavelength in the medium corresponding to the global maximum of P_{mean}. Fig. 10a, b and 10c display P_{mean} as a function of $\frac{\lambda}{5.3}$ for each gravel piles, assuming a value $\underline{\varepsilon}_{pile} = 6$. The global maximum is highlighted by a grey vertical dotted line. The error bars are, as in simulations, the standard deviations of P_{mean} computed on the set of soundings (11 soundings for pile a, 14 for pile b and 10 for pile c). Though less readily interpretable than the simulated ones, each curve shows a different frequency dependence. We focus, as previously explained, on the area of the global maximum of each curve, which also stands out because of its associated smaller error bars. The other parts of the curves, where the error bars are larger, show no clear trend with wavelength.

According to these observations, the ranges of values where we should retrieve L are.

a Pile a (Fig. 10a): λ_{peak} possibly exceeds the range of possible values. If so, L_a is beyond 3 cm. Based on the increasing values of P_{mean} on the right-hand side of the plot (dark arrow), we identify a lower bound value for L_a: $L_a \geq 2.7$ cm. We also note a local maximum around 1 cm (light grey arrow), which could be due to the typical size of the voids between the gravels. Those voids are typically 1-cm wide and could be seen by WISDOM as a second and smaller scatterer population in the pile. In the other piles (*b* and *c*), the voids are too small to be identified on the curves.
b Pile b (Fig. 10b): 1.6 cm$\leq L_b \leq$ 2.6 cm.
c Pile c (Fig. 10c): The global maximum indicates: 0.8 cm$\leq L_c \leq$ 1.4 cm. A thin local maximum is also remarkable around 1.9 cm (light grey arrow), its origin is not understood.

We then derived from the best-fit polynomial in these areas (except for gravel *a* whose maximum is possibly out of frame) the position of the global maximum backscatter and the associated uncertainty as explained in section 3.1. We obtain.

a Pile a (Fig. 10a): $L_a \geq 2.7$ cm (no polynomial fit is possible)
b Pile b (Fig. 10b): $L_b = 2.2 \pm 0.3$ cm
c Pile b (Fig. 10b): $L_c = 1.1 \pm 0.2$ cm

The position of estimated maximum is represented on Figs. 10b and c by the grey dotted line, and the black rectangle show the associated uncertainties.

The retrievals of L_b and L_c are in agreement with the actual typical sizes of gravels *b* and *c*, as illustrated by Fig. 10d. In contrast, gravels *a* are slightly too large to be well characterized in term of size, only a lower bound but still consistent with the actual values.

Discussion about these results will be presented in section 4.4.

4. Discussion

We have demonstrated that the typical size of heterogeneities can be retrieved using the same simple relation for all the heterogenous media we considered. In this section, we now investigate the robustness and limits of the method.

4.1. Range of size values that can be determined by the method

This method allows to retrieve the size of heterogeneities L if their value lies between $\frac{\lambda_{min}}{5.3}$ and $\frac{\lambda_{max}}{5.3}$, with $\lambda_{min} = \frac{c}{f_N\sqrt{\underline{\varepsilon}}}$ and $\lambda_{max} = \frac{c}{f_1\sqrt{\underline{\varepsilon}}}$, where f_1 and f_N are respectively the central frequencies of the first and last positions of the sliding window. For $\underline{\varepsilon} = 5$ and for a typical sliding window bandwidth $SW_{BW} = 200$ MHz, this translates into $\lambda_{min} = 4.6$ cm and $\lambda_{max} = 22.4$ cm which implies that the size L of heterogeneities WISDOM is sensitive to, is between 0.9 cm and 4.2 cm. For a GPR operating at lower frequencies, the size of heterogeneities that could be detected and characterized is larger. Fig. 11 is a color scaled map of the typical size L that could be retrieved for any mean effective permittivity value in the range $\underline{\varepsilon} = [1.2-10]$ and for any frequency value in the range [10 −4000] MHz. The horizontal arrows display the frequency ranges for WISDOM and for the two GPR already operated on Mars (RoPeR/Tianwen-1, RIMFAX/Mars2020).

4.2. Impact of $\frac{\Delta\varepsilon}{\underline{\varepsilon}}$ values on the validity domain

Due to the limitation of radar sensitivity, in order to apply the proposed method to estimate the L value , P_{mean} value must be above the noise level. In the case of WISDOM, P_{mean} must be above −66 dB. We thus define $\left[\frac{\Delta\varepsilon}{\underline{\varepsilon}}\right]_{threshold}$ the threshold permittivity relative contrast value for a given mean permittivity $\underline{\varepsilon}$ such as $P_{mean}\left(\left[\frac{\Delta\varepsilon}{\underline{\varepsilon}}\right]_{threshold}\right) = -66$ dB. Simulations performed on heterogeneous media with a very small permittivity contrast led to the threshold value $\left[\frac{\Delta\varepsilon}{\underline{\varepsilon}}\right]_{threshold} = 2.5 \times 10^{-2}$. This value is consistent with (Van Dam et al., 2003) which have already noticed that the minimum required textural variation necessary to produce GPR reflections is small. For such small permittivity contrast values (i.e., very slight variations in composition or porosity in the subsurface), the method remains valid and the relation $L = \lambda_{peak}/5.3$ that provides the value is unchanged.

On the other hand, we conducted simulations on relative permittivity contrast values up to $\frac{\Delta\varepsilon}{\underline{\varepsilon}} = 0.84$ (e.g., $\Delta\varepsilon = 4, \underline{\varepsilon} = 4.8$). The maximum of scattering intensity is still reached for the value of $\frac{\lambda_{peak}}{L}$. Nevertheless, high contrasts generate strong scattering losses thus a strong decrease of the signal intensity with depth. As a result, P_{mean} is computed over a shorter range of time delay, and the statistical deviation of P_{mean} is higher than for lower $\frac{\Delta\varepsilon}{\underline{\varepsilon}}$. This phenomenon occurs regardless of the mean permittivity $\underline{\varepsilon}$ that have been tested (within the explored range of values).

The value $\frac{\Delta\varepsilon}{\underline{\varepsilon}} = 0.84$ roughly corresponds to the maximum value

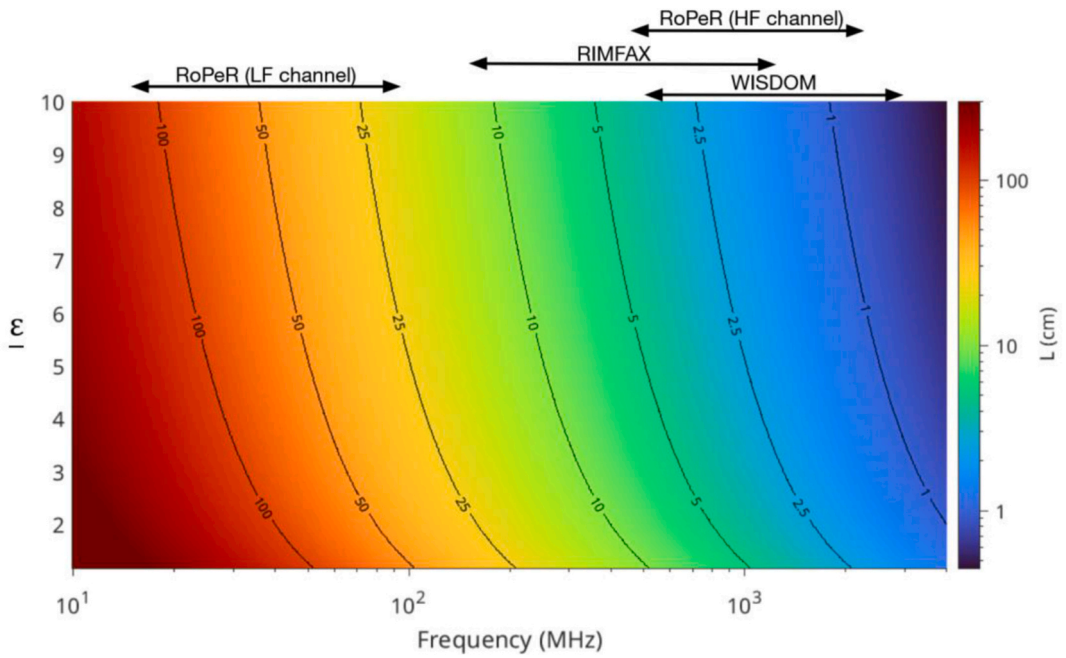

Fig. 11. Map of the typical size L that can be retrieved as a function of the mean effective permittivity $\underline{\varepsilon}$ of the subsurface (vertical axis) and of the frequency of the GPR (horizontal axis). The frequency ranges of operation of the two channels of RoPeR/Tianwen-1, of RIMFAX/Mars2020 and of WISDOM/ExoMars are indicated by the black arrows. The value of $L = \frac{\lambda_{peak}}{5.3}$ is given by the logarithmic color scale. (For interpretation of the references to color in this figure legend, the reader is referred to the Web version of this article.)

expected on Mars or on the Moon according to the values of real part of the permittivity reported in Table 1 Appendix. Higher values of $\frac{\Delta\varepsilon}{\underline{\varepsilon}}$ may exist and should be investigated but this would require smaller mesh size to avoid numerical divergence or slow convergence of the solution during FDTD simulation (Hirono et al., 2000; Kunz and Luebbers, 1993; Taflove, 1995).

4.3. Impact of electrical losses

In the previous sections, the investigated media were considered loss-less ($\varepsilon'' = 0$). However natural materials can be lossy. The imaginary part of the permittivity can vary over several orders of magnitude; in particular it increases with moisture. On Mars and on the Moon, liquid water is neither stable at the surface, nor in the first meters of the subsurface because of very low-pressure conditions. We therefore expect ε'' values to be lower than those measured on terrestrial rock analogs. Nevertheless, our current knowledge of ε'' for Martian and Lunar terrains remains limited; ε'' values published in the literature are estimated either from laboratory measurements performed on samples or derived from recent GPR observations (see Table 1 in Appendix). Note that in GPR studies we generally indifferently refer to ε'' or to the loss tangent defined as: $tan\ \delta = \frac{\varepsilon''}{\varepsilon}$.

In presence of electric losses and/or scatterers in the subsurface, the power density of the signal decreases exponentially along the propagating axis (vertically down-looking in the subsurface for GPR), hence with the depth z. We denote κ_a the power attenuation or extinction coefficient due to absorption by the material, and κ_s the extinction coefficient due to scattering within the medium. Both losses contribute to the exponential decrease of the power density ($\propto e^{-(\kappa_a+\kappa_s)z}$) and depend on the wavelength λ (or wavenumber k) of the wave propagating in the medium. As a consequence, both losses impact the frequency content of the signal. κ_a also depends on the real and imaginary parts of the effective permittivity as follows:

$$\kappa_a = \frac{4\pi}{\lambda}\left\{\frac{1}{2}\left[\sqrt{1+\left(\frac{\varepsilon''}{\varepsilon}\right)^2}-1\right]\right\}^{1/2} \quad (1)$$

Most of the materials in Table 1 in Appendix have a loss tangent small enough ($tan\ \delta < 10^{-2}$) to be regarded as low-loss materials, which simplifies the expression of κ_a at first order using Taylor's series:

$$\kappa_a \approx \frac{2\pi\varepsilon''}{\lambda\varepsilon} = \frac{2\pi}{\lambda} tan\ \delta = k{\cdot}tan\ \delta \quad (2)$$

According to equations (1) and (2), higher frequency content is more attenuated than lower one. As a result, the vertical resolution of GPR radargrams gets degraded with depth. This degradation adds to the variations of the frequency content due to the presence of heterogeneities of a given size. In this sub-section, we assess the influence of electrical losses on the frequency analysis presented in the previous sections, for a range of ε'' values chosen in agreement with the state of art (Table 1 in Appendix).

Most rocks and materials in the table are laboratory-made simulants of Martian and Lunar soils, and their ε" values strongly depend on the density, porosity, temperature, moisture and impurities, but they appear to vary between 0.001 and 0.3. JSC Mars-1 contains palagonitic tephra, a glassy volcanic ash altered at low temperature that was mined from a quarry at the Pu'u Nene volcanic cone, on the southern flank of Mauna Kea in Hawai'I (Allen et al., 1998). The iron oxide content of the volatile-free JSC Mars-1 is relatively close to the values of 15.6 wt% measured by the Viking and Pathfinder landers on Mars (Banin et al., 1992; Rieder et al., 1997). Clays may be the less transparent material at WISDOM frequencies. It must be considered since extended clay-bearing units are expected in Oxia Planum, the landing site of the ExoMars/Rosalind Franklin mission (Quantin-Nataf et al., 2021).

Measurements of the permittivity of the Moon regolith samples returned by the Apollo missions have been conducted for decades and ε'' values are therefore well constrained (Carrier et al., 1991). Samples from Mars will not be available before the completion of the Mars Sample Return mission now planned after 2030 (Muirhead et al., 2020).

In addition, losses have been estimated from *in situ* GPR data on the

Moon (with LPR/Chang'e−3 and LPR/Chang'e4; Ding et al., 2020; Li et al., 2020) and on Mars (with RIMFAX/Mars, 2020; Eide et al., 2022), at frequencies close to those of WISDOM by applying the centroid frequency-shift (CFS) method (first described in Quan and Harris, 1997). The CFS method relies on the fact that the centroid of the signal spectrum experiences a downshift during propagation into a lossy medium. However, if the medium is heterogenous, attenuation due to absorption and volume scattering being both frequency dependent, the CFS method rather provides an estimate of the total attenuation which includes both absorption and scattering attenuations. The derived and published loss tangent values must therefore be interpreted as a "global loss tangent". Consequently the ε'' values estimated on the Moon and on Mars and reported in Table 1 Appendix must be regarded as upper bounds for the imaginary part of permittivity. For comparison, the extinction coefficient computed based on RIMFAX/Mars 2020 data is $\kappa_{\text{Jezero}} = 2.6 \pm 0.3$ [dB /m] at the 675 MHz center frequency, whereas the extinction coefficient due only to volume scattering obtained from the simulations we performed on loss-less heterogeneous media is $\kappa_{\text{fractal}} \approx 1.3$ [dB /m] for relatively low permittivity contrast $\left(\frac{\Delta\varepsilon}{\underline{\varepsilon}} \leq 0.2\right)$ and rises up to $\kappa_{\text{fractal}} \approx 4.5$ [dB /m] for high permittivity contrast $\left(\frac{\Delta\varepsilon}{\underline{\varepsilon}} \geq 0.6\right)$. The attenuation rate caused by volume scattering is therefore of the same order of magnitude than the global attenuation measured on Mars near Jezero crater.

In addition to attenuation, another effect of electrical losses is to shift the position of the maximum volume scattering towards smaller values of kL (see Fig. 12, equations (1) and (2)). This leads to an underestimation of the scatterer size L. As shown in Fig. 11, when ε'' reaches 0.1 to 0.2, the maximum even disappears or cannot be unambiguously identified. We therefore define $\varepsilon''_{max} = 0.1$ as an upper limit for the imaginary part of the permittivity value for which the method we propose to retrieve L remains valid. The method is thus reliable and robust for most materials presented in Table 1 Appendix and for ε'' values measured on the Moon. Indeed Fig. 12 shows only a slight degradation of the curve shape for $\varepsilon'' \leq 0.05$. For clays and Mars JSC-1, ε'' may exceed ε''_{max}, but, as explained above, the ε'' value retrieved from RIMFAX data in Jezero crater, namely 0.13 (Eide et al., 2022), must be regarded as an upper limit and is likely smaller than ε''_{max}.

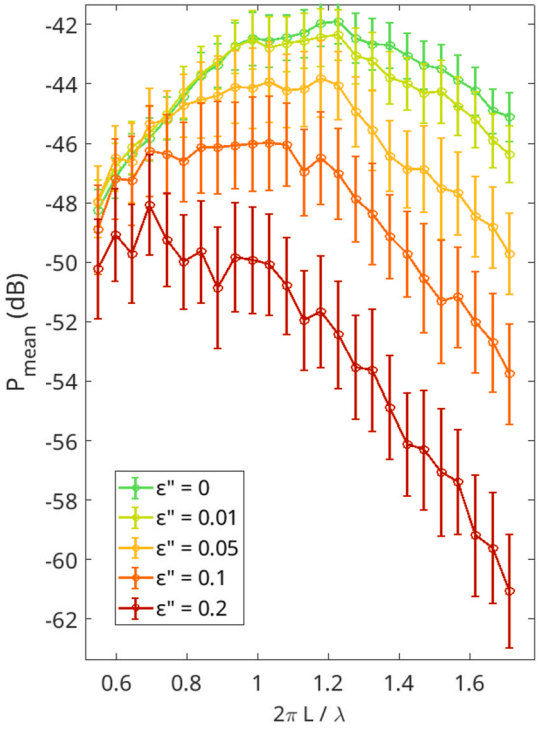

Fig. 12. P_{mean} as a function of kL for $(L, \Delta\varepsilon, \underline{\varepsilon}) = (1.4\,\text{cm}, 0.3, 5)$ and for increasing values of the imaginary part of the permittivity ε'' (from 0 to 0.2). The location of the maximum volume scattering is shifted to smaller values of kL with ε'' and tends to disappear when $\varepsilon'' > 0.1 - 0.2$.

4.4. Experimental result summary and discussion

The method applied to the experimental data (section 3.2.2.) made it possible to use the WISDOM data to provide constraints on the size of the gravels, which are consistent with the actual size ranges.

However, assumptions about the permittivity value of the gravel were necessary. Considering that $\underline{\varepsilon}_{pile} = 6$, the dry gravel case, is a lower bound for the bulk permittivity of the medium, the propagating wavelengths are therefore likely overestimated and, as a consequence, the values of L_a, L_b and L_c given in section 3.2.2. are likely upper bounds. The other extreme case to be explored is the moisty gravel case, where $\underline{\varepsilon}_{pile} = 10$ (Arcone et al., 2003). For the sake of clarity, the diagram in Fig. 13 compares the retrieved typical sizes in both extreme cases with the true gravel sizes.

The retrievals of L_b and L_c are in agreement with the real typical sizes of gravels *b* and *c*, as illustrated by Fig. 13. In contrast, gravels *a* are slightly too large to be well characterized in term of size ($L_a = 3.2$ cm is close or can be above $\frac{\lambda_{max}}{5.3} \in [2.5 - 3.3]$ cm). Nevertheless, the curve (Fig. 12) suggests the lower bound $L_a \geq 2.7$ cm, which is consistent with the actual size of gravels *a* (Fig. 13).

The gravel pile volumes being only a few cubic meters, the number of "uncorrelated" soundings we could perform with WISDOM was limited. Larger piles allowing more soundings might reduce the error bars.

In summary, despite an experimental field relatively different from the simulated heterogeneous media, a limited number of soundings and a limited penetration depth, the analysis of $P_{mean}\left(\frac{\lambda}{5.3}\right)$ provides valuable clues about the typical size of the gravels and establishes unambiguously that the three investigated piles are composed of scatterers of different typical size.

5. Conclusion and perspectives

The frequency analysis of the backscattered signal conducted on a statistical number of fractal heterogeneous media reveals a maximum reached at $\lambda_{peak} \approx 5.3\,L$, regardless the value of L and the permittivity distribution in the sounded volume. Any broad band GPR can be used to retrieve this typical size $L = \frac{\lambda_{peak}}{5.3}$ as long as the scatterers size commensurate with the GPR wavelengths of operation. For a mean permittivity $\underline{\varepsilon} = 9$ as measured by RIMFAX on Mars in Jezero crater (Hamran et al., 2022), WISDOM can be used to retrieve size L in the range [0.6–3.1] cm. For a mean permittivity $\underline{\varepsilon} = 3.2$ as measured by RoPeR on Mars in Utopia Planitia (Zou et al., 2024), this range is [1.1–5.3] cm. Lower frequency GPR will be sensitive to larger size of heterogeneities. It is essential to note that the determination of the size of the scatterers with this method does not require *a priori* knowledge of the permittivity distribution in the subsurface, which makes it easily useable when analyzing experimental data in an unknown environment.

The method we proposed in this paper is inevitably affected by electrical losses that are frequency dependent. However, simulations show that it is only slightly altered in most materials relevant to the Moon or Mars. Further, if the imaginary part of the permittivity of the sounded medium is known (for instance based on laboratory measurements on returned samples), we could apply a factor $e^{\kappa_a z}$ to correct the data from the absorption losses. In such cases, the method to retrieve L can be applied even for relatively high value of ε''.

The method has been tested and remains valid in simulation for relative permittivity contrast up to $\frac{\Delta\varepsilon}{\underline{\varepsilon}} = 0.84$. Simulation on higher

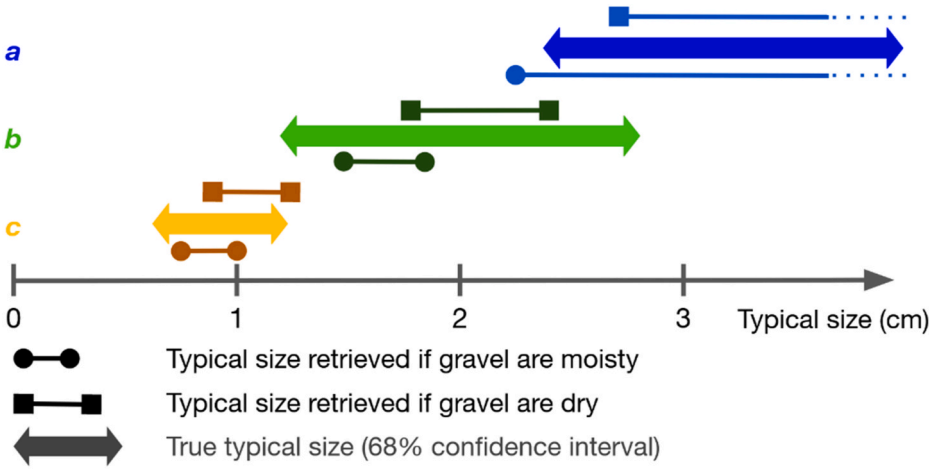

Fig. 13. For each gravel pile, comparison between the true sizes of the gravels and the retrieved typical sizes by our method. The retrieved size depends on the assumed permittivity of the piles. Results are here given for both the "moist gravel" (circles bounded line, with $\varepsilon_{pile} = 10$) and "dry gravels" (squares bounded line, with $\varepsilon_{pile} = 6$) cases.

permittivity contrast should be considered in future studies. For WISDOM dynamic range, simulations show that even an extremely small permittivity contrast can be discriminated from noise $\left(\left[\frac{\Delta\varepsilon}{\varepsilon}\right]_{threshold} = 2.5\times10^{-2}\right)$ and used for retrieving L, allowing to constrain the spatial scale of very subtle changes of composition or porosity in the investigated subsurface.

Further studies on volume scattering by a statistical number of buried spheres or ellipsoids are ongoing. Such studies can be useful for e.g. the characterisation of the permittivity values for streambed pebbles. The effect of volume scattering on cross-polarized measurements is also under investigation.

Future works will include testing the method on other well controlled or documented environments. The method will also be applied on field test campaign data; for instance, collected in 2019 in the Atacama Desert, Chile; in 2017 in Colorado Provençal, France; in 2022 on Svalbard, Norway; and in 2023 on Lanzarote, Canary Island, Spain. Ultimately, it will be used to analyze observations on Mars from present GPR and WISDOM.

CRediT authorship contribution statement

E. Brighi: Writing – review & editing, Writing – original draft, Visualization, Validation, Software, Methodology, Investigation, Formal analysis, Data curation, Conceptualization. **V. Ciarletti:** Writing – review & editing, Writing – original draft, Visualization, Supervision, Project administration, Methodology, Formal analysis, Conceptualization. **A. Le Gall:** Writing – review & editing, Writing – original draft, Visualization, Supervision, Project administration, Methodology, Formal analysis, Conceptualization. **D. Plettemeier:** Writing – review & editing, Project administration. **Y. Hervé:** Software, Resources. **N. Oudart:** Writing – review & editing, Software, Resources. **C. Quantin-Nataf:** Writing – review & editing, Resources. **M. Gilles:** Software. **F.-W. de Lamberterie:** Conceptualization.

Declaration of competing interest

The authors declare that they have no known competing financial interests or personal relationships that could have appeared to influence the work reported in this paper.

Acknowledgments

The authors wish to thank CNES, the French space agency for supporting the WISDOM instrument development. EB was funded by the French minister of research (MESR).

Appendix

Table 1
Imaginary part of the permittivity measured on Martian and Lunar simulants/samples or estimated from GPR data acquired on the Moon or on Mars

From laboratory measurements on simulants samples			
	ε	ε''	Frequency (GHz)
Mars JSC-1[1]	2–2.8	0.03 - 0.15	1.75
Mars JSC-1[2]	3.1	0.18	1.24
Carbondale Red Clay[2]	2.5-3.5	0.17 - 0.37	1.24
Dry sand deposits[2]	2–3	0.008	1.24
Dry sandstones[3]	3–5	0.001 - 0.03	0.45 - 1.2
Dry clays[3]	6–9	0.02 - 0.3	0.45 - 1.2
Tephra deposits[3]	3–5	0.01 - 0.15	0.45 - 1.2
Basalt[4]	6.2	0.0005	1.2
CO_2 & volcanic ash soil[4]	2	0.0004	1.2

(*continued on next page*)

Table 1 (*continued*)

From laboratory measurements on simulants samples			
	ε	ε''	Frequency (GHz)
From GPR measurements ε'' is obtained from published ε values and loss tangent $tan\,\delta$ values $\varepsilon'' = \varepsilon \times tan\,\delta$			
Moon (LPR/Chang'e−3)[5]	2–5	0.032 − 0.049	0.5
Moon (LPR/Chang'e−4)[8]	3.5	0.01–0.024	0.5
Mars (RIMFAX/Mars, 2020)	8.9 ± 3.2[10]	< 0.13[7]	0.675
Mars (RoPeR/Tianwen-1)	$3 - 3.4$[11]	< 0.057[9]	1.3
From laboratory measurements on returned samples			
Moon[6]	3–9	0.0006 - 0.023	0.45

1. 23 different Mars JSC-1 samples (Brouet et al., 2019).
2 (Williams, 2004).
3 (Ciarletti et al., 2017).
4 (Pettinelli et al., 2007).
5. Derived from LPR data in Ziwei crater (Ding et al., 2020).
6. Returned regolith samples by the Apollo missions (Carrier et al., 1991).
7. Derived from RIMFAX data in Jezero Crater (Eide et al., 2022).
8. Derived from LPR data on basalt mare at the lunar far side (Li et al., 2020).
9. Derived from RoPeR data in Utopia Planitia (Zhang et al., 2023).
10 (Casademont et al., 2023).
11 (Zou et al., 2024).

Data availability

Data will be made available on request.

References

Allen, C.C., Jager, K.M., Morris, R.V., Lindstrom, D.J., Lindstrom, M.M., Lockwood, J.P., 1998. Martian soil stimulant available for scientific, educational study. Eos Trans. Am. Geophys. Union 79, 405. https://doi.org/10.1029/98EO00309, 405.

Altieri, F., Frigeri, A., Lavagna, M., Le Gall, A., Yuryevich Nikiforov, S., Stoker, C., Ciarletti, V., Cristina De Sanctis, M., Josset, J.-L., Mitrofanov, I., Sefton-Nash, E., Vago, J.L., 2023. Investigating the Oxia Planum subsurface with the ExoMars rover and drill. Adv. Space Res. S0273117723000844. https://doi.org/10.1016/j.asr.2023.01.044.

Arcone, S.A., Peapples, P.R., Liu, L., 2003. Propagation of a ground-penetrating radar (GPR) pulse in a thin-surface waveguide. Geophysics 68, 1922–1933. https://doi.org/10.1190/1.1635046.

Banin, A., Clark, B.C., Waenke, H., 1992. Surface Chemistry and mineralogy., Mars.

Berenger, J.-P., 1994. A perfectly matched layer for the absorption of electromagnetic waves. J. Comput. Phys. 114, 185–200. https://doi.org/10.1006/jcph.1994.1159.

Besse, S., 2004. ÉTUDE Théorique De Radars Géologiques : analyses de sols, d'antennes et interprétation des signaux.

Blower, J.D., Keating, J.P., Mader, H.M., Phillips, J.C., 2003. The evolution of bubble size distributions in volcanic eruptions. J. Volcanol. Geoth. Res. 120, 1–23. https://doi.org/10.1016/S0377-0273(02)00404-3.

Bohren, C.F., Huffman, D.R., 1983. Absorption and Scattering of Light by Small Particles, A Wiley Interscience Publication, New York, 1983, vol. 25. G Mie Ann Phys, p. 351.

Brouet, Y., Becerra, P., Sabouroux, P., Pommerol, A., Thomas, N., 2019. A laboratory-based dielectric model for the radar sounding of the martian subsurface. Icarus 321, 960–973. https://doi.org/10.1016/j.icarus.2018.12.029.

Carrier III, W.D., Olhoeft, G.R., Mendell, W., 1991. Physical Properties of the Lunar Surface, Lunar Sourcebook. A User's Guide to the Moon.

Casademont, T.M., Eide, S., Shoemaker, E.S., Liu, Y., Nunes, D.C., Russell, P., Dypvik, H., Amundsen, H.E.F., Berger, T., Hamran, S.-E., 2023. RIMFAX ground penetrating radar reveals dielectric permittivity and rock density of shallow martian subsurface. J. Geophys. Res. Planets 128, e2022JE007598. https://doi.org/10.1029/2022JE007598.

Ciarletti, V., Clifford, S., Plettemeier, D., Le Gall, A., Hervé, Y., Dorizon, S., Quantin-Nataf, C., Benedix, W.-S., Schwenzer, S., Pettinelli, E., Heggy, E., Herique, A., Berthelier, J.-J., Kofman, W., Vago, J.L., Hamran, S.-E., the WISDOM Team, 2017. The WISDOM radar: unveiling the subsurface beneath the ExoMars rover and identifying the best locations for drilling. Astrobiology 17, 565–584. https://doi.org/10.1089/ast.2016.1532.

Ciarletti, V., Corbel, C., Plettemeier, D., Cais, P., Clifford, S.M., Hamran, S.-E., 2011. WISDOM GPR designed for shallow and high-resolution sounding of the martian subsurface. Proc. IEEE 99, 824–836. https://doi.org/10.1109/JPROC.2010.2100790.

Coates, A.J., Jaumann, R., Griffiths, A.D., Leff, C.E., Schmitz, N., Josset, J.-L., Paar, G., Gunn, M., Hauber, E., Cousins, C.R., Cross, R.E., Grindrod, P., Bridges, J.C., Balme, M., Gupta, S., Crawford, I.A., Irwin, P., Stabbins, R., Tirsch, D., Vago, J.L., Theodorou, T., Caballo-Perucha, M., Osinski, G.R., the PanCam Team, 2017. The PanCam instrument for the ExoMars rover. Astrobiology 17, 511–541. https://doi.org/10.1089/ast.2016.1548.

Dai, Q., Lee, Y.H., Sun, H.-H., Ow, G., Yusof, M.L.M., Yucel, A.C., 2022. DMRF-UNet: A Two-Stage Deep Learning Scheme for GPR Data Inversion under Heterogeneous Soil Conditions.

De Sanctis, M.C., Altieri, F., Ammannito, E., Biondi, D., De Angelis, S., Meini, M., Mondello, G., Novi, S., Paolinetti, R., Soldani, M., Mugnuolo, R., Pirrotta, S., Vago, J. L., the Ma_MISS team, 2017. Ma_MISS on ExoMars: mineralogical characterization of the martian subsurface. Astrobiology 17, 612–620. https://doi.org/10.1089/ast.2016.1541.

Ding, C., Xiao, Z., Su, Y., Zhao, J., Cui, J., 2020. Compositional variations along the route of Chang'e-3 Yutu rover revealed by the lunar penetrating radar. Prog. Earth Planet. Sci. 7, 32. https://doi.org/10.1186/s40645-020-00340-4.

Dorizon, S., Ciarletti, V., Plettemeier, D., Benedix, W.S., 2016. Performance validation of the ExoMars 2018 WISDOM GPR in ice caves, Austria. Planet. Space Sci. 120, 1–14. https://doi.org/10.1016/j.pss.2015.10.008.

Dorizon, S., Ciarletti, V., Vieau, A.-J., Plettemeier, D., Benedix, W.-S., Mütze, M., Hassen-Kodja, R., Humeau, O., 2014. WISDOM GPR Subsurface Investigations in the Atacama Desert during the SAFER Rover Operation Simulation, 16078.

Eide, S., Casademont, T.M., Berger, T., Dypvik, H., Shoemaker, E.S., Hamran, S., 2022. Radar attenuation in the shallow martian subsurface: RIMFAX time-frequency analysis and constant-Q characterization over Jezero Crater floor. Geophys. Res. Lett. https://doi.org/10.1029/2022GL101429.

Farley, K.A., Williford, K.H., Stack, K.M., Bhartia, R., Chen, A., De La Torre, M., Hand, K., Goreva, Y., Herd, C.D.K., Hueso, R., Liu, Y., Maki, J.N., Martinez, G., Moeller, R.C., Nelessen, A., Newman, C.E., Nunes, D., Ponce, A., Spanovich, N., Willis, P.A., Beegle, L.W., Bell, J.F., Brown, A.J., Hamran, S.-E., Hurowitz, J.A., Maurice, S., Paige, D.A., Rodriguez-Manfredi, J.A., Schulte, M., Wiens, R.C., 2020. Mars 2020 mission overview. Space Sci. Rev. 216, 142. https://doi.org/10.1007/s11214-020-00762-y.

Feitor, B., Caldeirinha, R., Fernandes, T., Ferreira, D., Leonor, N., 2011. Estimation of dielectric concrete properties from power measurements at 18.7 and 60 GHz. In: 2011 Loughborough Antennas & Propagation Conference. Presented at the Propagation Conference (LAPC), pp. 1–5. https://doi.org/10.1109/LAPC.2011.6114146. IEEE, Loughborough, United Kingdom.

Guiffaut, C., Reineix, A., Pecqueux, B., 2012. New oblique thin wire formalism in the FDTD method with multiwire junctions. IEEE Trans. Antenn. Propag. 60, 1458–1466. https://doi.org/10.1109/TAP.2011.2180304.

Hamran, S.-E., Paige, D.A., Allwood, A., Amundsen, H.E.F., Berger, T., Brovoll, S., Carter, L., Casademont, T.M., Damsgård, L., Dypvik, H., Eide, S., Fairén, A.G., Ghent, R., Kohler, J., Mellon, M.T., Nunes, D.C., Plettemeier, D., Russell, P., Siegler, M., Øyan, M.J., 2022. Ground penetrating radar observations of subsurface structures in the floor of Jezero crater, Mars. Sci. Adv. 8, eabp8564. https://doi.org/10.1126/sciadv.abp8564.

Hervé, Y., 2018. Le radar WISDOM à bord du Rover de la mission ExoMars: Caractérisation et préparation du retour scientifique.

Hervé, Y., Ciarletti, V., Le Gall, A., Corbel, C., Hassen-Khodja, R., Benedix, W.S., Plettemeier, D., Humeau, O., Vieau, A.J., Lustrement, B., Abbaki, S., Bertran, E., Lapauw, L., Tranier, V., Oudart, N., Vivat, F., Statz, C., Lu, Y., Hegler, S., Hérique, A., 2020. The WISDOM radar on board the ExoMars 2022 Rover: characterization and calibration of the flight model. Planet. Space Sci. 189, 104939. https://doi.org/10.1016/j.pss.2020.104939.

Hirono, T., Shibata, Y., Lui, W.W., Seki, S., Yoshikuni, Y., 2000. The second-order condition for the dielectric interface orthogonal to the Yee-lattice axis in the FDTD

scheme. IEEE Microw. Guid. Wave Lett. 10, 359–361. https://doi.org/10.1109/75.867850.
Holland, R., Simpson, L., 1981. Finite-Difference analysis of EMP coupling to thin struts and wires. IEEE Trans. Electromagn C. EMC-23, 88–97. https://doi.org/10.1109/TEMC.1981.303899.
Josset, J.-L., Westall, F., Hofmann, B.A., Spray, J., Cockell, C., Kempe, S., Griffiths, A.D., De Sanctis, M.C., Colangeli, L., Koschny, D., Föllmi, K., Verrecchia, E., Diamond, L., Josset, M., Javaux, E.J., Esposito, F., Gunn, M., Souchon-Leitner, A.L., Bontognali, T. R.R., Korablev, O., Erkman, S., Paar, G., Ulamec, S., Foucher, F., Martin, P., Verhaeghe, A., Tanevski, M., Vago, J.L., 2017. The close-up imager onboard the ESA ExoMars rover: objectives, description, operations, and science validation activities. Astrobiology 17, 595–611. https://doi.org/10.1089/ast.2016.1546.
Kunz, K.S., Luebbers, R.J., 1993. The Finite Difference Time Domain Method for Electromagnetics. CRC press.
Lai, J., Xu, Y., Zhang, X., Tang, Z., 2016. Structural analysis of lunar subsurface with Chang'E-3 lunar penetrating radar. Planet. Space Sci. 120, 96–102. https://doi.org/10.1016/j.pss.2015.10.014.
Le Gall, A., 2007. Sondage des sous-sols planétaires par radar à pénétration de sol: étude et modélisation des performances de l'instrument TAPIR. Paris 6.
Li, C., Liu, J., Ren, X., Zuo, W., Tan, X., Wen, W., Li, H., Mu, L., Su, Y., Zhang, H., Yan, J., Ouyang, Z., 2015. The Chang'e 3 Mission Overview. Space Sci. Rev. 190, 85–101. https://doi.org/10.1007/s11214-014-0134-7.
Li, C., Su, Y., Pettinelli, E., Xing, S., Ding, C., Liu, J., Ren, X., Lauro, S.E., Soldovieri, F., Zeng, X., Gao, X., Chen, W., Dai, S., Liu, D., Zhang, G., Zuo, W., Wen, W., Zhang, Z., Zhang, X., Zhang, H., 2020. The Moon's farside shallow subsurface structure unveiled by Chang'E-4 Lunar Penetrating Radar. Sci. Adv. 6, eaay6898. https://doi.org/10.1126/sciadv.aay6898.
Li, C., Zheng, Y., Wang, X., Zhang, J., Wang, Y., Chen, L., Zhang, L., Zhao, P., Liu, Yike, Lv, W., Liu, Yang, Zhao, X., Hao, J., Sun, W., Liu, X., Jia, B., Li, J., Lan, H., Fa, W., Pan, Y., Wu, F., 2022. Layered subsurface in utopia basin of Mars revealed by Zhurong rover radar. Nature. https://doi.org/10.1038/s41586-022-05147-5.
Li, Y., Zhou, B., Shen, S., Lu, W., Tang, C., Li, S., Su, Y., Dai, S., Fang, G., 2022. The lunar regolith structure and electromagnetic properties of Chang'E-5 landing site. Rem. Sens. 14, 4539. https://doi.org/10.3390/rs14184539.
Lognonné, P., Banerdt, W.B., Giardini, D., Pike, W.T., Christensen, U., Laudet, P., De Raucourt, S., Zweifel, P., Calcutt, S., Bierwirth, M., Hurst, K.J., Ijpelaan, F., Umland, J.W., Llorca-Cejudo, R., Larson, S.A., Garcia, R.F., Kedar, S., Knapmeyer-Endrun, B., Mimoun, D., Mocquet, A., Panning, M.P., Weber, R.C., Sylvestre-Baron, A., Pont, G., Verdier, N., Kerjean, L., Facto, L.J., Gharakanian, V., Feldman, J. E., Hoffman, T.L., Klein, D.B., Klein, K., Onufer, N.P., Paredes-Garcia, J., Petkov, M. P., Willis, J.R., Smrekar, S.E., Drilleau, M., Gabsi, T., Nebut, T., Robert, O., Tillier, S., Moreau, C., Parise, M., Aveni, G., Ben Charef, S., Bennour, Y., Camus, T., Dandonneau, P.A., Desfoux, C., Lecomte, B., Pot, O., Revuz, P., Mance, D., tenPierick, J., Bowles, N.E., Charalambous, C., Delahunty, A.K., Hurley, J., Irshad, R., Liu, H., Mukherjee, A.G., Standley, I.M., Stott, A.E., Temple, J., Warren, T., Eberhardt, M., Kramer, A., Kühne, W., Miettinen, E.-P., Monecke, M., Aicardi, C., André, M., Baroukh, J., Borrien, A., Bouisset, A., Boutte, P., Brethomé, K., Brysbaert, C., Carlier, T., Deleuze, M., Desmarres, J.M., Dilhan, D., Doucet, C., Faye, D., Faye-Refalo, N., Gonzalez, R., Imbert, C., Larigauderie, C., Locatelli, E., Luno, L., Meyer, J.-R., Mialhe, F., Mouret, J.M., Nonon, M., Pahn, Y., Paillet, A., Pasquier, P., Perez, G., Perez, R., Perrin, L., Pouilloux, B., Rosak, A., Savin de Larclause, I., Sicre, J., Sodki, M., Toulemont, N., Vella, B., Yana, C., Alibay, F., Avalos, O.M., Balzer, M.A., Bhandari, P., Blanco, E., Bone, B.D., Bousman, J.C., Bruneau, P., Calef, F.J., Calvet, R.J., D'Agostino, S.A., De Los Santos, G., Deen, R.G., Denise, R.W., Ervin, J., Ferraro, N.W., Gengl, H.E., Grinblat, F., Hernandez, D., Hetzel, M., Johnson, M.E., Khachikyan, L., Lin, J.Y., Madzunkov, S.M., Marshall, S. L., Mikellides, I.G., Miller, E.A., Raff, W., Singer, J.E., Sunday, C.M., Villalvazo, J.F., Wallace, M.C., Banfield, D., Rodriguez-Manfredi, J.A., Russell, C.T., Trebi-Ollennu, A., Maki, J.N., Beucler, E., Böse, M., Bonjour, C., Berenguer, J.L., Ceylan, S., Clinton, J., Conejero, V., Daubar, I., Dehant, V., Delage, P., Euchner, F., Estève, I., Fayon, L., Ferraioli, L., Johnson, C.L., Gagnepain-Beyneix, J., Golombek, M., Khan, A., Kawamura, T., Kenda, B., Labrot, P., Murdoch, N., Pardo, C., Perrin, C., Pou, L., Sauron, A., Savoie, D., Stähler, S., Stutzmann, E., Teanby, N.A., Tromp, J., Van Driel, M., Wieczorek, M., Widmer-Schnidrig, R., Wookey, J., 2019. SEIS: insight's seismic experiment for internal structure of Mars. Space Sci. Rev. 215, 12. https://doi.org/10.1007/s11214-018-0574-6.
Luebbers, R., Steich, D., Kunz, K., 1993. FDTD calculation of scattering from frequency-dependent materials. IEEE Trans. Antenn. Propag. 41, 1249–1257.
Mangold, N., Gupta, S., Gasnault, O., Dromart, G., Tarnas, J.D., Sholes, S.F., Horgan, B., Quantin-Nataf, C., Brown, A.J., Le Mouélic, S., Yingst, R.A., Bell, J.F., Beyssac, O., Bosak, T., Calef, F., Ehlmann, B.L., Farley, K.A., Grotzinger, J.P., Hickman-Lewis, K., Holm-Alwmark, S., Kah, L.C., Martinez-Frias, J., McLennan, S.M., Maurice, S., Nuñez, J.I., Ollila, A.M., Pilleri, P., Rice, J.W., Rice, M., Simon, J.I., Shuster, D.L., Stack, K.M., Sun, V.Z., Treiman, A.H., Weiss, B.P., Wiens, R.C., Williams, A.J., Williams, N.R., Williford, K.H., 2021. Perseverance rover reveals an ancient delta-lake system and flood deposits at Jezero crater, Mars. Science 374, 711–717. https://doi.org/10.1126/science.abl4051.
Mie, G., 1908. Pioneering mathematical description of scattering by spheres. Ann. Phys. 25, 3–3804.
Miller, G.S.P., 1986. The definition and rendering of terrain maps. In: Proceedings of the 13th Annual Conference on Computer Graphics and Interactive Techniques - SIGGRAPH '86. Presented at the the 13th Annual Conference. ACM Press, pp. 39–48. https://doi.org/10.1145/15922.15890. Not Known.
Muirhead, B.K., Nicholas, A., Umland, J., 2020. Mars sample return mission concept status. In: 2020 IEEE Aerospace Conference. Presented at the 2020 IEEE Aerospace Conference. Big Sky, IEEE, pp. 1–8. https://doi.org/10.1109/AERO47225.2020.9172609. MT, USA.
Oudart, N., 2021. Assessment of Processing and Interpretation Tools in Preparation of the WISDOM/ExoMars Ground Penetrating Radar Operations on Mars. Université Paris-Saclay.
Paige, D.A., Hamran, S.-E., Amundsen, H.E.F., Berger, T., Russell, P., Kakaria, R., Mellon, M.T., Eide, S., Carter, L.M., Casademont, T.M., Nunes, D.C., Shoemaker, E.S., Plettemeier, D., Dypvik, H., Holm-Alwmark, S., Horgan, B.H.N., 2024. Ground penetrating radar observations of the contact between the western delta and the crater floor of Jezero crater, Mars. Sci. Adv. 10, eadi8339. https://doi.org/10.1126/sciadv.adi8339.
Pettinelli, E., Burghignoli, P., Pisani, A.R., Ticconi, F., Galli, A., Vannaroni, G., Bella, F., 2007. Electromagnetic propagation of GPR signals in martian subsurface scenarios including material losses and scattering. IEEE Trans. Geosci. Rem. Sens. 45, 1271–1281. https://doi.org/10.1109/TGRS.2007.893563.
Plettemeier, D., Hahnel, R., Hegler, S., Safaeinili, A., Plaut, J., Gaskell, B., Orosei, R., Cicchetti, A., Picardi, G., 2009. Numerical computation of radar echoes measured by MARSIS during phobos flybys. In: 2009 IEEE Radar Conference. Presented at the 2009 IEEE Radar Conference. IEEE, Pasadena, CA, pp. 1–6. https://doi.org/10.1109/RADAR.2009.4977091.
Quan, Y., Harris, J.M., 1997. Seismic attenuation tomography using the frequency shift method. Geophysics 62, 895–905. https://doi.org/10.1190/1.1444197.
Quantin-Nataf, C., Carter, J., Mandon, L., Thollot, P., Balme, M., Volat, M., Pan, L., Loizeau, D., Millot, C., Breton, S., Dehouck, E., Fawdon, P., Gupta, S., Davis, J., Grindrod, P.M., Pacifici, A., Bultel, B., Allemand, P., Ody, A., Lozach, L., Broyer, J., 2021. Oxia Planum: the landing site for the ExoMars "Rosalind Franklin" rover mission: geological context and prelanding interpretation. Astrobiology 21, 345–366. https://doi.org/10.1089/ast.2019.2191.
Rea, J., Knight, R., 1998. Geostatistical analysis of ground-penetrating radar data: a means of describing spatial variation in the subsurface. Water Resour. Res. 34, 329–339. https://doi.org/10.1029/97WR03070.
Rieder, R., Economou, T., Wänke, H., Turkevich, A., Crisp, J., Brückner, J., Dreibus, G., McSween, H.Y., 1997. The chemical composition of martian soil and rocks returned by the mobile alpha proton X-ray spectrometer: preliminary results from the X-ray mode. Science 278, 1771–1774. https://doi.org/10.1126/science.278.5344.1771.
Salat, C., Junge, A., 2010. Dielectric permittivity of fine-grained fractions of soil samples from eastern Spain at 200 MHz. Geophysics 75, J1–J9. https://doi.org/10.1190/1.3294859.
Spohn, T., Grott, M., Smrekar, S.E., Knollenberg, J., Hudson, T.L., Krause, C., Müller, N., Jänchen, J., Börner, A., Wippermann, T., Krömer, O., Lichtenheldt, R., Wisniewski, L., Grygorczuk, J., Fittock, M., Rheershemius, S., Spröwitz, T., Kopp, E., Walter, I., Plesa, A.C., Breuer, D., Morgan, P., Banerdt, W.B., 2018. The heat flow and physical properties package (HP3) for the InSight mission. Space Sci. Rev. 214, 96. https://doi.org/10.1007/s11214-018-0531-4.
Sullivan, D.M., 2013. Electromagnetic Simulation Using the FDTD Method. John Wiley & Sons.
Taflove, A., 1995. Computational Electrodynamics: the Finite-Difference Time-Domain Method. Artech House, Boston.
Taflove, A., Hagness, S.C., Piket-May, M., 2005. Computational electromagnetics: the finite-difference time-domain method. Electr. Eng. Handb. 3, 15.
Vago, J.L., Westall, F., Pasteur Instrument Teams, Landing S., Coates, A.J., Jaumann, R., Korablev, O., Ciarletti, V., Mitrofanov, I., Josset, J.-L., De Sanctis, M.C., Bibring, J.-P., Rull, F., Goesmann, F., Steininger, H., Goetz, W., Brinckerhoff, W., Szopa, C., Raulin, F., Westall, F., Edwards, H.G.M., Whyte, L.G., Fairén, A.G., Bibring, J.-P., Bridges, J., Hauber, E., Ori, G.G., Werner, S., Loizeau, D., Kuzmin, R.O., Williams, R. M.E., Flahaut, J., Forget, F., Vago, J.L., Rodionov, D., Korablev, O., Svedhem, H., Sefton-Nash, E., Kminek, G., Lorenzoni, L., Joudrier, L., Mikhailov, V., Zashchirinskiy, A., Alexashkin, S., Calantropio, F., Merlo, A., Poulakis, P., Witasse, O., Bayle, O., Bayón, S., Meierhenrich, U., Carter, J., García-Ruiz, J.M., Baglioni, P., Haldemann, A., Ball, A.J., Debus, A., Lindner, R., Haessig, F., Monteiro, D., Trautner, R., Voland, C., Rebeyre, P., Goulty, D., Didot, F., Durrant, S., Zekri, E., Koschny, D., Toni, A., Visentin, G., Zwick, M., van Winnendael, M., Azkarate, M., Carreau, C., the ExoMars Project Team, 2017. Habitability on early Mars and the search for biosignatures with the ExoMars rover. Astrobiology 17, 471–510. https://doi.org/10.1089/ast.2016.1533.
Van Dam, R.L., Van Den Berg, E.H., Schaap, M.G., Broekema, L.H., Schlager, W., 2003. Radar reflections from sedimentary structures in the vadose zone. Geol. Soc. Lond. Spec. Publ. 211, 257–273. https://doi.org/10.1144/GSL.SP.2001.211.01.21.
Van Der Baan, M., 2001. Acoustic wave propagation in one-dimensional random media: the wave localization approach. Geophys. J. Int. 145, 631–646. https://doi.org/10.1046/j.1365-246x.2001.01405.x.
Vasavada, A.R., 2022. Mission overview and scientific contributions from the Mars science laboratory curiosity rover after eight years of surface operations. Space Sci. Rev. 218, 14. https://doi.org/10.1007/s11214-022-00882-7.
Williams, K.K., 2004. Measurements of dielectric loss factors due to a Martian dust analog. J. Geophys. Res. 109, E10006. https://doi.org/10.1029/2002JE001957.
Williams, R.M.E., Grotzinger, J.P., Dietrich, W.E., Gupta, S., Sumner, D.Y., Wiens, R.C., Mangold, N., Malin, M.C., Edgett, K.S., Maurice, S., Forni, O., Gasnault, O., Ollila, A., Newsom, H.E., Dromart, G., Palucis, M.C., Yingst, R.A., Anderson, R.B., Herkenhoff, K.E., Le Mouélic, S., Goetz, W., Madsen, M.B., Koefoed, A., Jensen, J.K., Bridges, J.C., Schwenzer, S.P., Lewis, K.W., Stack, K.M., Rubin, D., Kah, L.C., Bell, J. F., Farmer, J.D., Sullivan, R., Van Beek, T., Blaney, D.L., Pariser, O., Deen, R.G., Msl Science Team, Kemppinen, O., Bridges, N., Johnson, J.R., Minitti, M., Cremers, D., Edgar, L., Godber, A., Wadhwa, M., Wellington, D., McEwan, I., Newman, C., Richardson, M., Charpentier, A., Peret, L., King, P., Blank, J., Weigle, G., Schmidt, M., Li, S., Milliken, R., Robertson, K., Sun, V., Baker, M., Edwards, C.,

Ehlmann, B., Farley, K., Griffes, J., Miller, H., Newcombe, M., Pilorget, C., Rice, M., Siebach, K., Stolper, E., Brunet, C., Hipkin, V., Léveillé, R., Marchand, G., Sobrón Sánchez, P., Favot, L., Cody, G., Steele, A., Flückiger, L., Lees, D., Nefian, A., Martin, M., Gailhanou, M., Westall, F., Israël, G., Agard, C., Baroukh, J., Donny, C., Gaboriaud, A., Guillemot, P., Lafaille, V., Lorigny, E., Paillet, A., Pérez, R., Saccoccio, M., Yana, C., Aparicio, C.A., Caride Rodríguez, J., Carrasco Blázquez, I., Gómez Gómez, F., Elvira, J.G., Hettrich, S., Lepinette Malvitte, A., Marín Jiménez, M., Frías, J.M., Soler, J.M., Torres, F.J.M., Molina Jurado, A., Sotomayor, L. M., Muñoz Caro, G., Navarro López, S., González, V.P., García, J.P., Rodriguez Manfredi, J.A., Planelló, J.J.R., Alejandra Sans Fuentes, S., Sebastian Martinez, E., Torres Redondo, J., O'Callaghan, R.U., Zorzano Mier, M.-P., Chipera, S., Lacour, J.-L., Mauchien, P., Sirven, J.-B., Manning, H., Fairén, A., Hayes, A., Joseph, J., Squyres, S., Thomas, P., Dupont, A., Lundberg, A., Melikechi, N., Mezzacappa, A., DeMarines, J., Grinspoon, D., Reitz, G., Prats, B., Atlaskin, E., Genzer, M., Harri, A.-M., Haukka, H., Kahanpää, H., Kauhanen, J., Paton, M., Polkko, J., Schmidt, W., Siili, T., Fabre, C., Wray, J., Wilhelm, M.B., Poitrasson, F., Patel, K., Gorevan, S., Indyk, S., Paulsen, G., Bish, D., Schieber, J., Gondet, B., Langevin, Y., Geffroy, C., Baratoux, D., Berger, G., Cros, A., Uston, C.D., Lasue, J., Lee, Q.-M., Meslin, P.-Y., Pallier, E., Parot, Y., Pinet, P., Schröder, S., Toplis, M., Lewin, É., Brunner, W., Heydari, E., Achilles, C., Oehler, D., Sutter, B., Cabane, M., Coscia, D., Szopa, C., Robert, F., Sautter, V., Nachon, M., Buch, A., Stalport, F., Coll, P., François, P., Raulin, F., Teinturier, S., Cameron, J., Clegg, S., Cousin, A., DeLapp, D., Dingler, R., Jackson, R.S., Johnstone, S., Lanza, N., Little, C., Nelson, T., Williams, R.B., Jones, A., Kirkland, L., Treiman, A., Baker, B., Cantor, B., Caplinger, M., Davis, S., Duston, B., Fay, D., Hardgrove, C., Harker, D., Herrera, P., Jensen, E., Kennedy, M.R., Krezoski, G., Krysak, D., Lipkaman, L., McCartney, E., McNair, S., Nixon, B., Posiolova, L., Ravine, M., Salamon, A., Saper, L., Stoiber, K., Supulver, K., Van Beek, J., Zimdar, R., French, K.L., Iagnemma, K., Miller, K., Summons, R., Goesmann, F., Hviid, S., Johnson, M., Lefavor, M., Lyness, E., Breves, E., Dyar, M.D., Fassett, C., Blake, D.F., Bristow, T., DesMarais, D., Edwards, L., Haberle, R., Hoehler, T., Hollingsworth, J., Kahre, M., Keely, L., McKay, C., Bleacher, L., Brinckerhoff, W., Choi, D., Conrad, P., Dworkin, J.P., Eigenbrode, J., Floyd, M., Freissinet, C., Garvin, J., Glavin, D., Harpold, D., Mahaffy, P., Martin, D.K., McAdam, A., Pavlov, A., Raaen, E., Smith, M.D., Stern, J., Tan, F., Trainer, M., Meyer, M., Posner, A., Voytek, M., Anderson, R.C., Aubrey, A., Beegle, L.W., Behar, A., Brinza, D., Calef, F., Christensen, L., Crisp, J.A., DeFlores, L., Feldman, J., Feldman, S., Flesch, G., Hurowitz, J., Jun, I., Keymeulen, D., Maki, J., Mischna, M., Morookian, J.M., Parker, T., Pavri, B., Schoppers, M., Sengstacken, A., Simmonds, J. J., Spanovich, N., De La Torre Juarez, M., Vasavada, A.R., Webster, C.R., Yen, A., Archer, P.D., Cucinotta, F., Jones, J.H., Ming, D., Morris, R.V., Niles, P., Rampe, E., Nolan, T., Fisk, M., Radziemski, L., Barraclough, B., Bender, S., Berman, D., Dobrea, E.N., Tokar, R., Vaniman, D., Leshin, L., Cleghorn, T., Huntress, W., Manhès, G., Hudgins, J., Olson, T., Stewart, N., Sarrazin, P., Grant, J., Vicenzi, E., Wilson, S.A., Bullock, M., Ehresmann, B., Hamilton, V., Hassler, D., Peterson, J., Rafkin, S., Zeitlin, C., Fedosov, F., Golovin, D., Karpushkina, N., Kozyrev, A., Litvak, M., Malakhov, A., Mitrofanov, I., Mokrousov, M., Nikiforov, S., Prokhorov, V., Sanin, A., Tretyakov, V., Varenikov, A., Vostrukhin, A., Kuzmin, R., Clark, B., Wolff, M., McLennan, S., Botta, O., Drake, D., Bean, K., Lemmon, M., Lee, E.M., Sucharski, R., Hernández, M.Á.D.P., Blanco Ávalos, J.J., Ramos, M., Kim, M.-H., Malespin, C., Plante, I., Muller, J.-P., González, R.N., Ewing, R., Boynton, W., Downs, R., Fitzgibbon, M., Harshman, K., Morrison, S., Kortmann, O., Williams, A., Lugmair, G., Wilson, M.A., Jakosky, B., Zunic, T.B., Frydenvang, J., Kinch, K., Stipp, S.L.S., Boyd, N., Campbell, J.L., Gellert, R., Perrett, G., Pradler, I., VanBommel, S., Jacob, S., Owen, T., Rowland, S., Savijärvi, H., Boehm, E., Böttcher, S., Burmeister, S., Guo, J., Köhler, J., García, C.M., Mellin, R.M., Schweingruber, R.W., McConnochie, T., Benna, M., Franz, H., Bower, H., Brunner, A., Blau, H., Boucher, T., Carmosino, M., Atreya, S., Elliott, H., Halleaux, D., Rennó, N., Wong, M., Pepin, R., Elliott, B., Spray, J., Thompson, L., Gordon, S., Williams, J., Vasconcelos, P., Bentz, J., Nealson, K., Popa, R., Moersch, J., Tate, C., Day, M., Kocurek, G., Hallet, B., Sletten, R., Francis, R., McCullough, E., Cloutis, E., Ten Kate, I.L., Arvidson, R., Fraeman, A., Scholes, D., Slavney, S., Stein, T., Ward, J., Berger, J., Moores, J.E., 2013. Martian fluvial conglomerates at Gale crater. Science 340, 1068–1072. https://doi.org/10.1126/science.1237317.

Wu, T., King, R., 1965. The cylindrical antenna with nonreflecting resistive loading. IEEE Trans. Antenn. Propag. 13, 369–373. https://doi.org/10.1109/TAP.1965.1138429.

Yee, K.S., 1966. Numerical solution of initial boundary value problems involving Maxwell's equations in isotropic meida. IEEE Trans. Antenn. Propag. 14, 1327–1333.

Zhang, L., Li, J., Zeng, Z., Xu, Y., Liu, C., Chen, S., 2020. Stratigraphy of the von kármán crater based on Chang'E-4 lunar penetrating radar data. Geophys. Res. Lett. 47. https://doi.org/10.1029/2020GL088680.

Zhang, L., Xu, Y., Liu, R., Chen, R., Bugiolacchi, R., Gao, R., 2023. The dielectric properties of martian regolith at the tianwen-1 landing site. Geophys. Res. Lett. 50, e2022GL102207. https://doi.org/10.1029/2022GL102207.

Zou, L., Liu, H., Alani, A.M., Fang, G., 2024. Surface permittivity estimation of southern utopia Planitia by high-frequency RoPeR in Tianwen-1 Mars exploration. IEEE Trans. Geosci. Rem. Sens. 62, 1–9. https://doi.org/10.1109/TGRS.2024.3370620.

Zou, Y., Zhu, Y., Bai, Y., Wang, L., Jia, Y., Shen, W., Fan, Y., Liu, Y., Wang, C., Zhang, A., Yu, G., Dong, J., Shu, R., He, Z., Zhang, T., Du, A., Fan, M., Yang, J., Zhou, B., Wang, Y., Peng, Y., 2021. Scientific objectives and payloads of Tianwen-1, China's first Mars exploration mission. Adv. Space Res. 67, 812–823. https://doi.org/10.1016/j.asr.2020.11.005.